Band-to-band Tunneling in Silicon Diodes and Tunnel Transistors

by

James Towfik Teherani
B.S. Electrical Engineering
The University of Texas at Austin, 2008

Submitted to the Department of Electrical Engineering and Computer Science
in Partial Fulfillment of the Requirements for the Degree of

Master of Science in Electrical Engineering and Computer Science
at the
Massachusetts Institute of Technology

June 2010

Signature of Author: _____
Department of Electrical Engineering and Computer Science
May 18, 2010

Certified by: _____
Judy L. Hoyt
Professor, Electrical Engineering and Computer Science
Thesis Supervisor

_____
Dimitri A. Antoniadis
Professor, Electrical Engineering and Computer Science
Thesis Supervisor

Accepted by: _____
Terry P. Orlando
Professor, Electrical Engineering and Computer Science
Chairman, Department Committee on Graduate Theses

Band-to-band Tunneling in Silicon Diodes and Tunnel Transistors

by

James Towfik Teherani

Submitted to the Department of Electrical Engineering and Computer Science
on May 18, 2010 in Partial Fulfillment of the Requirements for the Degree of
Master of Science in Electrical Engineering and Computer Science

Abstract

This work studies the effect of mechanically applied uniaxial strain on reverse-bias band-to-band tunneling current in n+/p+ vertical silicon diodes fabricated on {100} and {110} substrate orientations. The *Band Structure Lab* and *nextnano*^{3} are used to analyze the change in band structure with uniaxial stress applied perpendicular to the tunneling direction along <100> and <110> crystal directions. A theoretical analysis based on the Wentzel-Kramers-Brillouin (WKB) approximation for tunneling probability combined with an uncoupled full-band Poisson equation solver and the calculated band structure changes is developed to model the experimental results. Reasonable agreement between experimental data and theoretical calculations is found when comparing the relative change in tunneling current at 1 V reverse-bias versus strain for different substrate orientation/strain configurations.

Thesis Supervisors: Judy L. Hoyt, Professor of Electrical Engineering
Dimitri A. Antoniadis, Professor of Electrical Engineering

To Christy, my family, friends, and teachers

Table of Contents

List of Figures

List of Tables

Chapter 1: Motivation for Tunneling Field-Effect Transistor and Tunnel Diode Research

The great pace of the electronics industry can be attributed to the successful scaling of silicon transistors since the 1970s. However, beginning in the early 2000s, additional enhancement techniques beyond Dennard's scaling law [1] were required to push technology to the next development node. This was achieved through the application of strain engineering and by use of novel materials such as high-κ dielectrics and metal gates [2],[3]. Ultimately, the scaling of the traditional metal-oxide-semiconductor field-effect transistor (MOSFET) runs into serious roadblocks in the next ten years, and because of this many alternative transistor types are under investigation. In particular, new transistor operating principles, which can reduce power dissipation in integrated circuits, are of interest.

One type of alternative that has received attention is the tunneling field-effect transistor (TFET) [4]. Tunneling is a quantum mechanical effect where particles have a finite probability of transmission through an energy barrier due to their wave nature, and this effect becomes pronounced at nanometer length scales. Quantum mechanical tunneling is explained in depth in Chapter 2: *Introduction to Quantum Tunneling*. The TFET seeks to use tunneling as an advantageous effect, where carriers are injected through a barrier instead of over a thermal barrier, as in a conventional MOSFET. A comparison of an n-MOSFET and basic n-TFET structure is shown in Figure 1a and Figure 1b below.

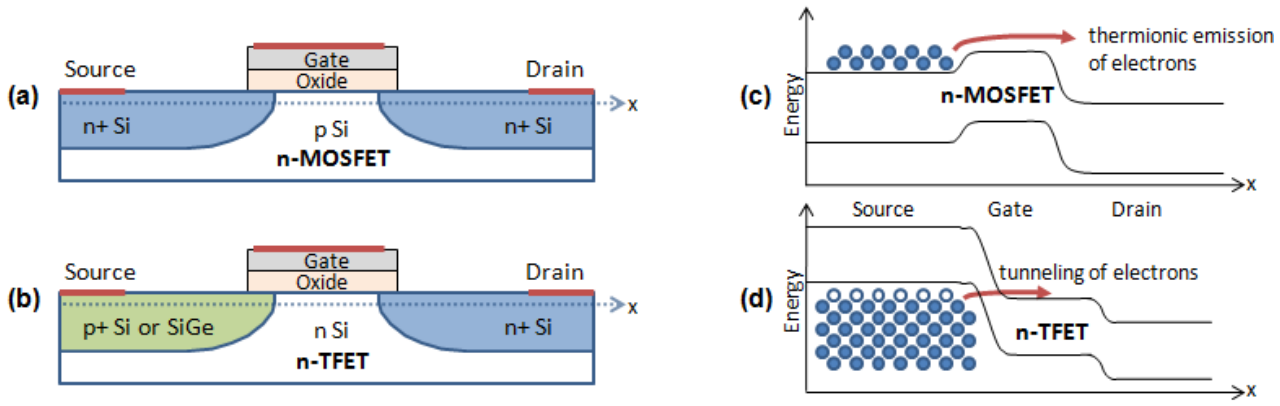

Figure 1. (a) Standard n-MOSFET structure. (b) n-TFET structure in which drain and source doping are no longer symmetrical. (c) Energy band diagram for the n-MOSFET in which current is carried by thermionic emission of electrons. (d) Energy band diagram for n-TFET in which gate voltage modulates the band-to-band tunneling barrier.

In this thesis, the tunneling diode is studied as a tool to better understand the effects of band structure on the band-to-band tunneling phenomena in the TFET devices. In both the TFET and the tunnel diode, band-to-band tunneling occurs between the valence band of a p-region and the conduction band of an n-region. The main difference between the devices is the use of a third terminal (the gate contact) to modulate tunneling in the TFET. In the tunnel diode, tunneling is modulated by changing the bias across the p-n tunnel junction. Contrary to the TFET, the tunnel diode is a one-dimensional structure which is easier to fabricate and provides fundamental insight into the tunneling mechanism and its dependence on semiconductor properties.

In this work, silicon vertical tunnel diodes were fabricated on different substrates. Since an applied bias creates a vertical electric field, tunneling occurs preferentially along the wafer's vertical crystallographic direction. Different substrate orientations allow different crystallographic tunneling paths to be studied. A comparison of tunneling current for different substrate orientations provides insight into a preferential tunneling direction for the silicon

crystal. Applied mechanical uniaxial strain alters the band structure of the device in predictable ways. The strain breaks the band degeneracy to allow the effects of each band to be separated. From a device performance view, applied strain can increase or decrease tunneling in a specified direction so that device performance can be optimized for the desired application. In this work, strain is used as an instrument to better understand band-to-band tunneling under various band structure conditions.

While the ultimate goal of the broader research is to produce a CMOS-compatible low power transistor compared to the MOSFET, much of the current work is targeted at better understanding the band-to-band tunneling phenomena in devices. This also has implications for current MOSFETs; gate-induced drain leakage (GIDL)—a parasitic band-to-band tunneling effect at the drain-substrate junction caused by large electric fields between the gate and drain regions—becomes more troubling with every technology generation as the oxide thickness shrinks and fields increase. Knowledge gained from tunnel diode research can be utilized to decrease unwanted tunneling in MOSFETs [5]. Moreover, tunneling research may lead to devices and structures not yet conceived.

1.1 Potential Advantages of the Tunneling Field-Effect Transistor Compared to Conventional MOSFETs

The TFET works by using the gate to modulate the width of a tunneling barrier, instead of the height of a barrier that carriers must surmount via thermionic emission. The transport of carriers in the n-MOSFET and n-TFET structures is depicted in Figure 1c and Figure 1d above. Since TFETs function via a tunneling mechanism, they have weak temperature dependence and potential for subthreshold swing below the kT/q thermal limit of 60 mV/decade at room

temperature [6]. It should be noted that indirect tunneling depends on phonon-electron interactions for the change in momentum from the Γ-valley maximum to the X-valley minimum. The phonon occupation obeys Bose-Einstein statistics, and the number of phonons *is* sensitive to temperature; however, indirect tunneling can occur even with a zero phonon occupancy due to phonon emission by the tunneling particle. For this reason, tunneling is not exponentially dependent on temperature, and the overall tunneling rate is proportional to $1 + 2N$, where N is the occupancy for phonons with the momentum required for the indirect transition [7].

A steep subthreshold swing allows for lower supply voltage V_{DD}, and thus low power device operation, as power scales as the square of V_{DD}. A device with a steep subthreshold swing requires less gate voltage for a given on-current to off-current ratio. The TFET research seeks to reduce the power dissipation of electronics while improving performance.

TFETs are not plagued by the same short channel effects as MOSFETs. Although the drain potential can affect the tunneling barrier at very short channel lengths, a reduction in V_{DD} enabled by the steep subthreshold swing of a TFET can likely lessen the effect. Therefore, the TFET device structure potentially allows for scaling to shorter channel lengths prolonging Moore's Law, and these properties make TFETs a candidate for ultra-low power logic applications.

Chapter 2: Introduction to Quantum Tunneling

The concept of tunneling was first introduced with the advent of quantum mechanics in the second decade of the twentieth century. The quantum mechanical equations predict the wave nature of matter which asserts that matter exhibits wavelike properties under some conditions and particle-like properties under other conditions. The Schrödinger formulation of quantum mechanics presents an interesting phenomenon where a particle tunnels through an energy barrier, similar to evanescent wave coupling of electromagnetic waves [8]. The Schrödinger equation is given by

$$i\hbar\frac{\partial}{\partial t}\Psi(\boldsymbol{r},t) = \hat{H}\Psi(\boldsymbol{r},t) \tag{1}$$

where $\hbar$ is Planck's constant divided by 2π, $\Psi(\boldsymbol{r},t)$ is the wave function at position $\boldsymbol{r}$ and time t, and the Hamiltonian operator $\hat{H}$ is defined as

$$\hat{H} = -\frac{\hbar^2}{2m}\nabla^2 + V(\boldsymbol{r},t) \tag{2}$$

$V(\boldsymbol{r},t)$ is the potential energy that can vary with space and time. For a particle traveling in free space without any potentials, $V(\boldsymbol{r},t)$ is taken to be zero. Under these conditions, a plane wave of the form $\Psi(\boldsymbol{r},t) = e^{i(kx-\omega t)}$ satisfies Equation (1) above where the wave vector k is 2π divided by the wavelength, and the angular frequency ω is 2π times the frequency.

For tunneling through a potential barrier, the problem is simplified by using the method of separation of variables. With this method, a solution of the form $\Psi(\boldsymbol{r},t) = R(r)T(t)$ is assumed which allows the problem to be broken up into a time-dependent and time-independent problem. $R(r)$ is the spatial component and $T(t)$ is the temporal component of the wave

function. The time-dependent problem is easily solved, leaving only the time-independent solution to be found. The time-independent Schrödinger problem for one-dimension becomes

$$E\psi(x) = -\frac{\hbar^2}{2m}\frac{d^2}{dx^2}\psi(x) + V(x)\psi(x) \tag{3}$$

where E is the energy and $\psi(x)$ is the spatial component of the wave function along x. The combined wave function is given by

$$\psi(x,t) = \psi(x)e^{-\left(\frac{iEt}{\hbar}\right)} \tag{4}$$

Moreover, a time-independent plane wave solution of the form $\psi(x) = e^{ikx}$ satisfies Equation (3) for any constant potential V_0 in space. Plugging in the plane wave solution yields the condition that

$$k = \sqrt{\frac{2m(E - V_0)}{\hbar^2}} \tag{5}$$

2.1 Tunneling in One-Dimension

The problem of a particle impinging on a rectangular potential barrier is drawn in Figure 2. The particle is represented by an incident forward propagating plane wave with amplitude A_{x+} and energy E traveling in a material with zero potential. A second material exists from $x = 0$ to $x = d$ with a potential V_0 such that $0 < E < V_0$.

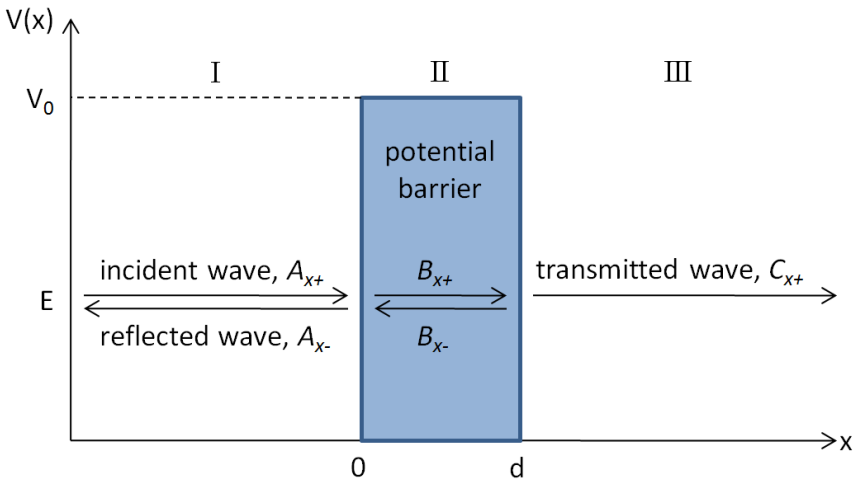

Figure 2. Plane wave incident on a rectangular potential barrier. A portion of the incident wave is transmitted and the rest is reflected at the potential barrier.

A forward propagating wave and a backward propagating wave is assumed in regions I and II due to reflection off the surfaces at $x = 0$ and $x = d$. No backward propagating wave is assumed for region III because no surface exists to reflect the forward-propagating transmitted wave. Using these assumptions as a starting point, an equation of the form below is assumed as the solution to the time-independent Schrödinger equation:

$$\psi(x) = \begin{cases} A_{x+} \cdot e^{ik_I x} + A_{x-} \cdot e^{-ik_I x}, & \text{for } x \leq 0 \\ B_{x+} \cdot e^{ik_{II} x} + B_{x-} \cdot e^{-ik_{II} x}, & \text{for } 0 \leq x \leq d \\ C_{x+} \cdot e^{ik_{III} x}, & \text{for } x \geq d \end{cases} \tag{6}$$

Additionally, the following boundary conditions must be true for a valid wave function solution:

$$\psi_I(0) = \psi_{II}(0) \tag{7}$$

$$\psi_{II}(d) = \psi_{III}(d) \tag{8}$$

$$\frac{d}{dx}\psi_I(0) = \frac{d}{dx}\psi_{II}(0) \tag{9}$$

$$\frac{d}{dx}\psi_{II}(d) = \frac{d}{dx}\psi_{III}(d) \tag{10}$$

Using Equation (5), the wave vectors are found to be

$$k_I = k_{III} = \sqrt{\frac{2mE}{\hbar^2}} \tag{11}$$

$$k_{II} = \sqrt{\frac{2m(E - V_0)}{\hbar^2}} = i\sqrt{\frac{2m(V_0 - E)}{\hbar^2}} = -i\kappa \tag{12}$$

where

$$\kappa = -\sqrt{\frac{2m(V_0 - E)}{\hbar^2}} = ik_{II} \tag{13}$$

κ is a real number since $V_0 > E$ in region II. Substituting Equation (12) into Equation (6), one finds that in the barrier (region II), the wave function is composed of exponential terms:

$$\begin{aligned} \psi_{II}(x) &= B_{x+} \cdot e^{ik_{II}x} + B_{x-} \cdot e^{-ik_{II}x} \\ &= B_{x+} \cdot e^{+\kappa x} + B_{x-} \cdot e^{-\kappa x} \end{aligned} \tag{14}$$

Taking the incident amplitude A_{x+} to be unity, one can solve the set of four equations: Equations (7)-(10) and four unknowns: $A_{x-}, B_{x+}, B_{x-}, C_{x+}$. The transmission probability $T(E)$ can be calculated as the square of the absolute value of the amplitude of the transmitted wave since the initial and final k-vectors are the same:

$$T(E) = |C_{x+}|^2 = \frac{4E(V_0 - E)}{4E(V_0 - E) + V_0^2 \sinh^2\left(\pi\sqrt{\frac{V_0 - E}{E_d}}\right)} \tag{15}$$

where

$$E_d = \frac{\hbar^2\pi^2}{2md^2} \tag{16}$$

From this quantum mechanical analysis, a nonzero transmission coefficient is calculated for a particle with energy less than the barrier height. The particle is able to tunnel through the barrier with a finite probability. This is forbidden in classical mechanics as it would require the particle to have a negative kinetic energy since the total particle energy is the sum of the kinetic energy and potential energy; however, quantum mechanics shows that tunneling is a valid solution to the Schrödinger equation, and thus, a real phenomenon of particles.

2.2 Band-to-band Tunneling in Diodes

The tunneling of interest in this thesis is band-to-band tunneling in silicon diodes and TFETs. For band-to-band tunneling to occur, an electron in the valence band of the semiconductor tunnels across the band gap to the conduction band without the assistance of traps as shown in Figure 3. The band gap acts as the potential barrier that the particle tunnels across. For direct tunneling, an electron travels from the valence band to the conduction band without the absorption or emission of a phonon.

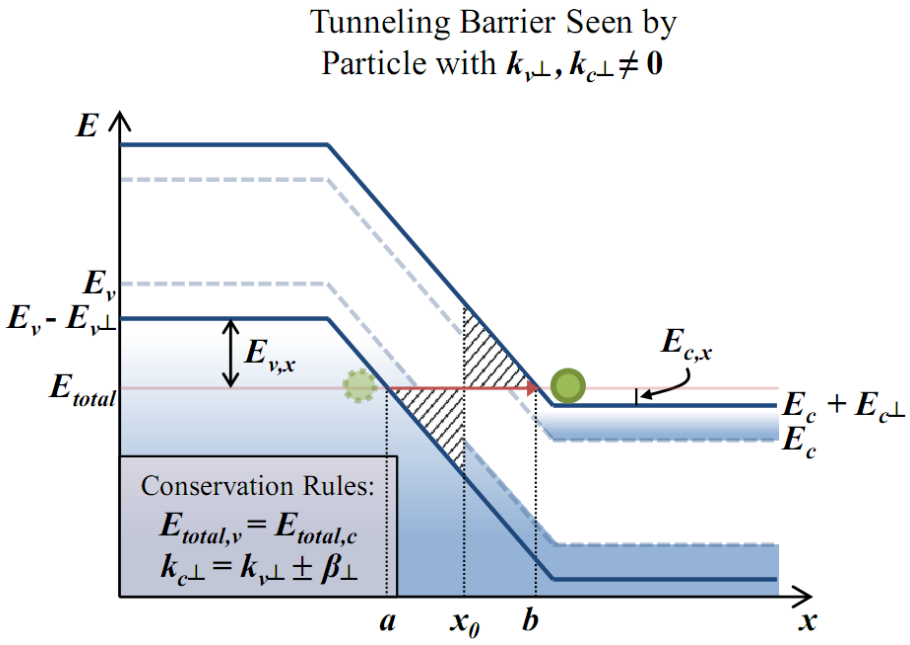

Figure 3. Energy band diagram for a p-n diode with band-to-band tunneling. A particle with nonzero perpendicular momentum (as defined by momentum oriented within the plane of the junction) tunnels across the band gap from the valence band at $x = a$ to the conduction band at $x = b$. The transition from valence band-like properties to conduction band-like properties occurs at $x = x_0$, and the overall tunneling barrier is indicated by the hatched areas.

In the indirect tunneling process, a tunneling particle acquires a change in momentum by absorbing or emitting a phonon. Indirect tunneling is the main tunneling process in indirect semiconductors whose gamma-centered direct band gap, E_Γ, is much greater than their indirect band gap, E_G, as is the case with silicon where E_Γ = 3.4 eV and E_G = 1.12 eV [9]. The full band structure for silicon is shown in Figure 4. The direct tunneling process is negligible in silicon because the transmission probability decreases rapidly with increasing barrier height as seen in Equation (15). The electron tunneling through the band gap is akin to a particle tunneling through a potential barrier, and the most probable tunneling path is through the smallest barrier, which results in the two triangular barriers drawn in Figure 3 above.

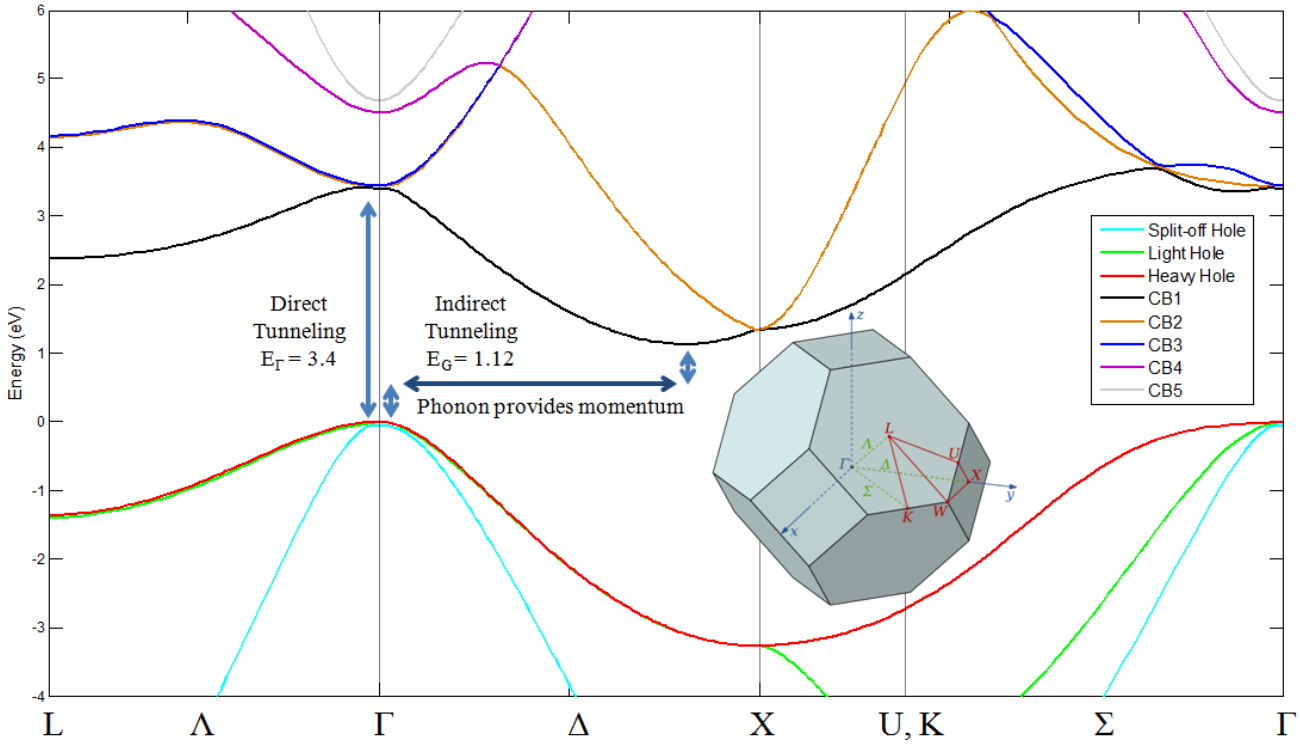

Figure 4. Full band structure of unstrained silicon calculated using [10]. The inset shows the first Brillouin zone for an FCC lattice with points of high symmetry indicated. Inset image from [11].

Figure 3 depicts band-to-band tunneling for a heavily doped p+/n+ diode with a constant electric field across the junction. An incident valence band electron with energy in the *x*-direction tunnels across the band gap to a state in the conduction band. The electron tunnels from the valence band at $x = a$ to the conduction band at $x = b$, and the phonon interaction for a transition from valence band-like properties to conduction band-like properties occurs at $x = x_0$. The tunneling barrier is indicated by the hatched areas in the figure. Perpendicular momentum increases the action integral of the potential barrier, defined below in Equation (19), and thus causes tunneling to decrease. For direct tunneling, the requirement for conservation of perpendicular momentum causes an increase in the tunneling path shown in Figure 5. A particle with some perpendicular momentum in the valence band must tunnel to a state with the same perpendicular momentum in the conduction band, which results in a longer tunneling path.

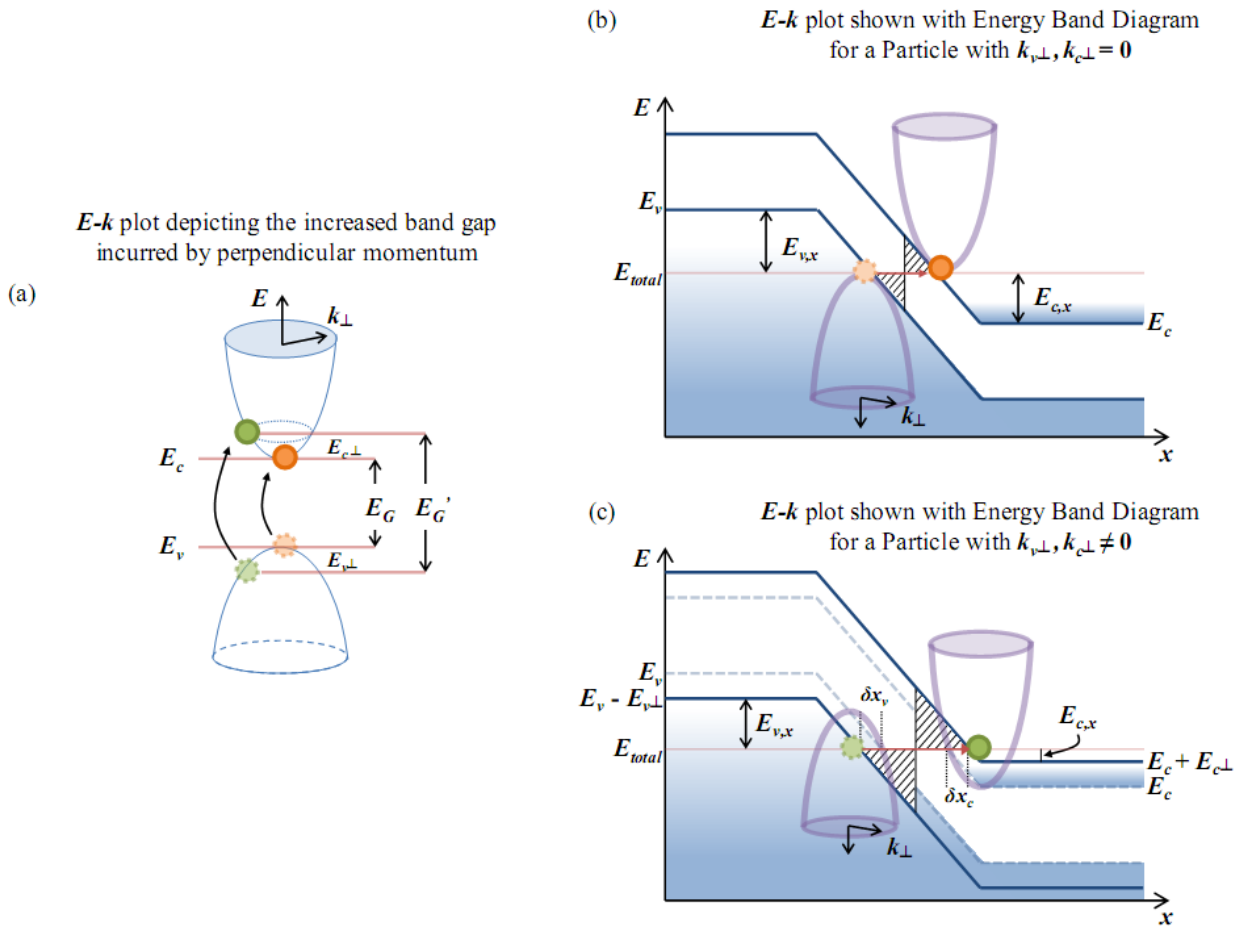

Figure 5. (a) *E-k* plot depicting the increased band gap incurred by perpendicular momentum. (b) Band diagram of a p-n diode for a tunneling electron with zero perpendicular momentum in the valence band and conduction band. (c) Band diagram for a tunneling electron with non-zero perpendicular momentum in the valence band and conduction band. The perpendicular momentum causes an increase in the tunneling path as depicted. Both (b) and (c) have an *E-k* diagram superimposed on the band diagram to show the effect of perpendicular momentum.

It should be noted that in the indirect tunneling process, the phonon *does* impart or absorb a change in the momentum of the particle. Therefore, the electron-phonon interaction of the indirect tunneling process decouples the perpendicular momentum of valence band and conduction band. An electron in the valence band can tunnel to any state in the conduction band such that total energy and perpendicular momentum are conserved:

$$E_{total} = E_{c0,n} + \frac{\hbar^2 k_c^2}{2m_c^*} = E_{v0,p} - \frac{\hbar^2 k_v^2}{2m_v^*} \pm \hbar\omega_\beta \tag{17}$$

$$k_{c\perp} = k_{v\perp} \pm \beta_\perp \tag{18}$$

In Equation (18), β is the wave vector of the phonon. Under the continuum approximation, β can be any value so that $k_{c\perp}$ is independent of $k_{v\perp}$. However, the energy imparted for a momentum transfer from the Γ-valley maximum to the X-valley minimum by a transverse acoustic phonon is approximately 18 meV [12]. Because this energy is quite small, the approximation is made that no change in total energy occurs with the phonon interaction, and the term $\hbar\omega_\beta$ is neglected.

2.2.1 Equations for Band-to-band Tunneling in Diodes

The tunneling is calculated using the Wentzel-Kramers-Brillouin (WKB) approximation [13] which gives the transmission coefficient for a particle tunneling in the *x*-direction as

$$T \sim exp\left(-2\int_a^b \kappa_x \, dx\right) \tag{19}$$

The integral over dx is commonly referred to as the tunneling action integral—the larger the action integral, the smaller the transmission coefficient. For the case drawn in Figure 3, the particle transitions from an electron with valence band-like properties to an electron with conduction band-like properties at x_0. We rewrite Equation (19) to reflect this:

$$T \sim exp\left[-2\left(\int_a^{x_0} \kappa_{vx} \, dx + \int_{x_0}^b \kappa_{cx} \, dx\right)\right] \tag{20}$$

κ_{vx} and κ_{cx} are given by the following equations for an isotropic mass:

$$k_v = \sqrt{\frac{2m_v(E_v(x) - E)}{\hbar^2}}, \qquad k_c = \sqrt{\frac{2m_c(E - (E_v(x) + E_G))}{\hbar^2}} \tag{21}$$

$$\left\{ \begin{array}{ll} k_v^2 = k_{vx}^2 + k_{v\perp}^2 & \Rightarrow \quad k_{vx}^2 = k_v^2 - k_{v\perp}^2 \\ k_c^2 = k_{cx}^2 + k_{c\perp}^2 & \Rightarrow \quad k_{cx}^2 = k_c^2 - k_{c\perp}^2 \end{array} \right\} \tag{22}$$

$$\kappa_x = ik_x, \qquad \kappa_v = ik_v, \qquad \kappa_c = ik_c \tag{23}$$

$$\left(\frac{\kappa_{vx}}{i}\right)^2 = \left(\frac{\kappa_v}{i}\right)^2 - k_{v\perp}^2 \tag{24}$$

$$\left\{ \begin{array}{l} \kappa_{vx} = \sqrt{\kappa_v^2 + k_{v\perp}^2} \\ \kappa_{cx} = \sqrt{\kappa_c^2 + k_{c\perp}^2} \end{array} \right\} \tag{25}$$

This implies that the transmission coefficient can be rewritten in terms of total momentum and perpendicular momentum as

$$T \sim exp\left[-2\left(\int_a^{x_0} \sqrt{\kappa_v^2 + k_{v\perp}^2}\, dx + \int_{x_0}^{b} \sqrt{\kappa_c^2 + k_{c\perp}^2}\, dx\right)\right] \tag{26}$$

For a fixed energy, κ_v is constant by definition. Equation (26) shows that as transverse momentum $k_{v\perp}$ increases, the tunneling probability exponentially decreases for a constant κ_v (or a fixed total energy). This equation can be simplified by first factoring κ_v and κ_c out of the square root and then applying the Taylor series approximation that $\sqrt{1+\alpha} \approx 1 + \frac{1}{2}\alpha$, for $\alpha \ll 1$:

$$T \sim exp\left[-2\left(\int_a^{x_0} \kappa_v \sqrt{1 + \frac{k_{v\perp}^2}{\kappa_v^2}}\, dx + \int_{x_0}^{b} \kappa_c \sqrt{1 + \frac{k_{c\perp}^2}{\kappa_c^2}}\, dx\right)\right] \tag{27}$$

$$T \sim exp\left[-2\left(\int_a^{x_0} \kappa_v\, dx + \int_{x_0}^{b} \kappa_c\, dx\right) - \left(k_{v\perp}^2 \int_a^{x_0} \frac{1}{\kappa_v} dx + k_{c\perp}^2 \int_{x_0}^{b} \frac{1}{\kappa_c} dx\right)\right] \tag{28}$$

From Equation (25), it can be seen that $\kappa_v = \kappa_{vx}(k_{v\perp} = 0) \equiv \kappa_{vx,0}$. Equation (28) can be rewritten in terms of κ_{vx0} and κ_{cx0} so that the transmission coefficient becomes

$$T \sim exp\left[-2\left(\int_a^{x_0} \kappa_{vx,0}\, dx + \int_{x_0}^{b} \kappa_{cx,0}\, dx\right) - \left(k_{v\perp}^2 \int_a^{x_0} \frac{1}{\kappa_{vx,0}} dx + k_{c\perp}^2 \int_{x_0}^{b} \frac{1}{\kappa_{cx,0}} dx\right)\right] \quad (29)$$

The above equation can be written in terms of total energy and perpendicular momentum of the valence band and conduction band:

$$T(E, k_{v\perp}, k_{c\perp}) \sim exp\left[-2\left(\int_a^{x_0} \sqrt{\frac{2m_{vx}\left(E - E_v(x)\right)}{\hbar^2}}\, dx + \int_{x_0}^{b} \sqrt{\frac{2m_{cx}\left((E_v(x) + E_G) - E\right)}{\hbar^2}}\, dx\right) - \left(k_{v\perp}^2 \int_a^{x_0} \frac{1}{\kappa_{vx,0}} dx + k_{c\perp}^2 \int_{x_0}^{b} \frac{1}{\kappa_{cx,0}} dx\right)\right] \quad (30)$$

For the constant field assumption, the energy of the valence band as a function of position is given by

$$E_v(x) = E_{v0} + qFx \quad (31)$$

where the electric field, F, is negative for the case drawn in Figure 3 above. Additionally, the integral in Equation (30) is minimized when $\kappa_{vx,0}(x_0) = \kappa_{cx,0}(x_0)$ which leads to

$$x_0 = \frac{1}{qF}\left(E - E_{v0} - \frac{m_{cx}}{m_{cx} + m_{vx}} E_G\right) \quad (32)$$

With this information, the integrals in Equation (30) can be calculated:

$$T(k_{v\perp},k_{c\perp})\sim exp\left[-2\left(-\frac{2}{3}\frac{(E_G)^{1.5}}{qF\hbar}\sqrt{\frac{2m_{vx}m_{cx}}{m_{vx}+m_{cx}}}\right)\right.$$
$$\left.-\left(-\frac{\hbar k_{v\perp}^2}{qF}\sqrt{E_G\cdot\frac{2m_{cx}}{m_{vx}}\frac{1}{m_{cx}+m_{vx}}}-\frac{\hbar k_{c\perp}^2}{qF}\sqrt{E_G\cdot\frac{2m_{vx}}{m_{cx}}\frac{1}{m_{cx}+m_{vx}}}\right)\right] \quad (33)$$

(where F is negative)

This equation can be further condensed with some algebra to

$$T(k_{v\perp},k_{c\perp})\sim exp\left[-2\left(\frac{(E_G)^{0.5}}{q|F|\hbar}\sqrt{2m_r}\left[\frac{2}{3}E_G+\frac{1}{2}\left(\frac{\hbar^2k_{v\perp}^2}{m_{vx}}+\frac{\hbar^2k_{c\perp}^2}{m_{cx}}\right)\right]\right)\right] \quad (34)$$

where m_r is the reduced mass given by

$$m_r=\left(\frac{1}{m_{vx}}+\frac{1}{m_{cx}}\right)^{-1}=\frac{m_{vx}m_{cx}}{m_{vx}+m_{cx}} \quad (35)$$

Using this equation, the transmission probability of a particle at a specific energy can be calculated. When the perpendicular momentum of the particle in the valence band and conduction band is zero, the transmission coefficient is found to be

$$T(k_{v\perp}=0,k_{c\perp}=0)\sim exp\left[-\frac{4}{3}\frac{(E_G)^{1.5}}{q|F|\hbar}\sqrt{2m_r}\right] \quad (36)$$

which agrees with the general treatment of tunneling in various texts [14].

For direct tunneling, the perpendicular momentum of the particle in the conduction band must equal the perpendicular momentum of the particle in the valence band in order to conserve perpendicular momentum as no phonon interaction occurs. Under this constraint, Equation (34) is written as

Direct tunneling: $$T(E_{v\perp}) \sim exp\left[-2\left(\frac{(E_G)^{0.5}}{q|F|\hbar}\sqrt{2m_r}\left[\frac{2}{3}E_G + \frac{m_{v\perp}}{m_r}E_{v\perp}\right]\right)\right] \quad (37)$$

Although tunneling in silicon occurs through an indirect process, the direct tunneling equation is used in the theoretical analysis of this thesis. Both equations are similar; however the indirect formulation allows for additional freedom of the perpendicular momenta in the valence and conduction bands as they are no longer required to be equivalent. In both cases, tunneling is dominated by particles with little perpendicular momentum so Equation (37) is used to simplify the analysis. Equation (37) will become the basis for the tunneling current calculation described in Chapter 6: *Theoretical Current Calculation*.

Chapter 3: Fabrication and Sample Preparation

The silicon tunnel diodes were previously fabricated at the IBM T. J. Watson Research Center in Yorktown, Heights, New York. The author prepared the samples and performed measurements on the devices during the summer of 2009 while interning at IBM.

3.1 Device Fabrication

The fabrication of the silicon tunnel diodes was completed at the IBM T. J. Watson Research Center in Yorktown Heights, New York. The local oxidation of silicon (LOCOS) method was used to create isolated areas, and the wafers were ion implanted to form the p-n junction of the diode. A sketch of the structure is drawn in Figure 6. In the experiment, three different wafer orientations were used: [001], [011], and [111]. The different wafer orientations enable comparison of vertical tunneling along different crystallographic directions. For each of the three substrates, boron was implanted at 20 keV for eight different doses from 0.6×10^{14} to 7.5×10^{14} cm^{-2}. Additionally, a 2 keV arsenic implant was completed for all devices with a dose of 2.5×10^{15} cm^{-2} to create the n+ top of the vertical diode. Many junctions were short-circuited due to metal spiking through the shallow implant. The devices were reworked and received an additional arsenic dose of 2.5×10^{15} cm^{-2} at 20 keV to prevent spiking through the n-region. The dopants were ion implanted through a mask with various layout geometries, but this thesis only focuses on the 5 µm and 10 µm structures of squares and circles. After the implants, the devices underwent a rapid thermal anneal at 1050˚C for 5 seconds.

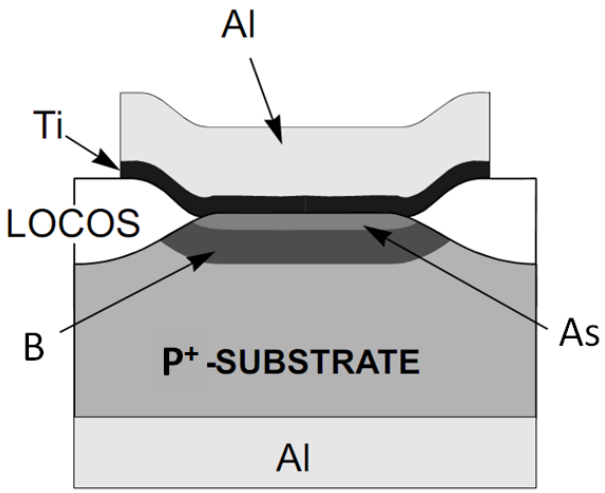

Figure 6. Vertical structure of the fabricated diodes. Image courtesy of P. Solomon, IBM [15].

3.2 Doping Profiles of Vertical Diodes

After fabrication, the doping profile of the p-n junction for the various ion implants was carefully studied by Solomon et. al. [5] through multiple techniques. TSUPREM simulation of the processing conditions yielded the results shown in Figure 7 below.

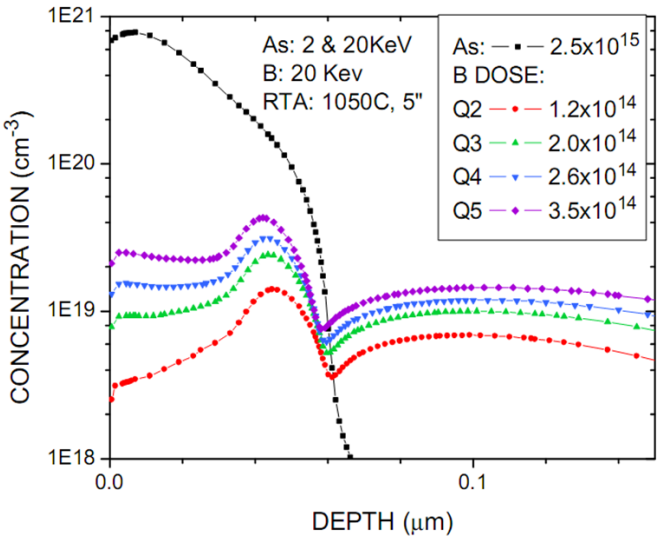

Figure 7. TSUPREM simulation of the vertical diode doping profile for different boron doses in units of cm^{-2}. Image courtesy of P. Solomon, IBM [5].

3.3 Sample Preparation

The samples were bent along various directions so that different uniaxial stresses could be studied. Two bending directions of interest were the ⟨100⟩ and ⟨110⟩ families of directions. The ⟨100⟩ direction involved the simplest analysis as stress was applied to a primary crystallographic axis. Stress was also applied to the ⟨110⟩ directions as an additional measurement.

In order to apply stress along the desired directions, the wafer was cut into rectangular sample pieces such that the long side of the sample was directed along the desired strain direction. The wafer was split into samples by either cleaving the wafer or by using a dice saw. Cleaving has the advantage that the resulting cleavage plane is nearly atomically smooth with minimum damage for a nicely cleaved piece; however, only certain directions lie along the wafer's cleavage planes, and cleaving must be done by hand with limited reproducibility. Wafer directions not lying along cleavage planes required the wafer to be sawed, creating mechanical damage along the path of the cut. Mechanical damage caused the stressed devices to break at a lower stress level.

In order to apply the maximum strain, wafers were cleaved along the desired bending directions if a cleavage plane existed. In the case that a cleavage plane did not exist for a specific direction, the sample was sawed along the direction followed by an isotropic silicon polishing etch to remove the saw damage.

3.3.1 Cleavage Planes

The crystallographic properties for each wafer orientation are listed in Table 1. Since wafer cleavage most likely occurs along {111} planes, the cleaving directions were calculated by the intersection of {111} planes with the wafer's surface plane, given by the wafer orientation. To

find the cleaving direction for a (001) wafer, the intersection of the (001) plane with the {111} family of cleavage planes is calculated by taking the cross product of the two planes. For example, the intersection of a (001) plane with a (111) plane is a line given by

$$(0\hat{x} + 0\hat{y} + 1\hat{z}) \times (1\hat{x} + 1\hat{y} + 1\hat{z}) = (-1\hat{x} + 1\hat{y} + 0\hat{z}) \quad (38)$$

This calculation shows that the $[\bar{1}10]$ direction is a cleaving direction for (001) wafers. Completing the above calculation for all planes in the {111} family shows that [110] is also a cleavage direction for (001) wafers.

Given Material Properties			Calculated	Desired
Wafer Orientation	**Notch Direction**	**Perpendicular to Notch Direction**	**Cleaving Directions**	**Bending Directions**
(001)	**[110]**	**$[\bar{1}10]$**	**<110>**	**<100>, <110>**
(011)	**[100]**	**$[01\bar{1}]$**	**<110>, <112>**	**<100>, <110>**
(111)	**$[\bar{1}10]$**	**$[\bar{1}\bar{1}2]$**	**<110>**	**<110>**

Table 1. Wafer orientations and desired bending directions.

The desired bending directions are shown in Table 1 above. A ⟨100⟩ bending direction does not exist on the surface plane of a (111) wafer. Therefore, ⟨100⟩ bending cannot be applied to (111) wafers. The ⟨100⟩ bending directions for (001) and (011) wafers required sawing of the samples, while the samples bent along the ⟨110⟩ direction were cleaved.

3.4 Silicon Polishing Etch

The samples required sawing in order to achieve some of the bending directions. An isotropic silicon polishing etch was used to remove the mechanical damage created on the sides of the

samples from the sawing process. Following the work of [16], an isotropic silicon etch was developed from a combination of nitric acid (HNO_3) and hydrofluoric acid (HF) to smooth out any roughness and damage created by the sawing process. Nitric acid oxidizes silicon creating silicon dioxide (SiO_2), and hydrofluoric acid subsequently dissolves the oxide. The intermediary reactions created during the oxidation of silicon are quite complicated as discussed in [17]; however simplified reactions are listed below:

Oxidation: $$3\,Si_{(s)} + 4\,HNO_{3_{(aq)}} \rightarrow 3\,SiO_{2_{(s)}} + 4\,NO_{(g)} + 2\,H_2O_{(l)} \quad (39)$$

Dissolution: $$SiO_{2_{(s)}} + 6\,HF_{(aq)} \rightarrow H_2SiF_{6_{(aq)}} + 2\,H_2O_{(l)} \quad (40)$$

Overall: $$3\,Si_{(s)} + 4\,HNO_{3_{(aq)}} + 18\,HF_{(aq)} \rightarrow 3\,H_2SiF_{6_{(aq)}} + 4\,NO_{(g)} + 8\,H_2O_{(l)} \quad (41)$$

The characteristics of the silicon etch are dependent on the concentration of nitric acid to hydrofluoric acid as shown in Figure 8. An etch solution with nitric acid as the limiting reactant produces anisotropic etching as the oxidation rate is very dependent on electron concentration. Therefore, the oxidation rate varies along different crystallographic planes due to dissimilar electron densities of the crystal planes resulting in anisotropic etching. Conversely, when nitric acid is in excess, the reaction is limited by the diffusion rate of hydrofluoric acid to the surface of the sample. Since diffusion proceeds through an isotropic mechanism, this reaction results in isotropic etching. However, Schwartz and Robbins show that at very low concentrations of hydrofluoric acid, the etch pattern becomes anisotropic as the etch rate drops [16]. To explain this behavior, they hypothesize that the reaction is autocatalytic with one of the oxidation reaction products acting as the catalyst. Recent research shows that intermediate nitrogen species play a large role in the reaction process, and more research is needed to clarify the etching of silicon in nitric acid and hydrofluoric solutions [17].

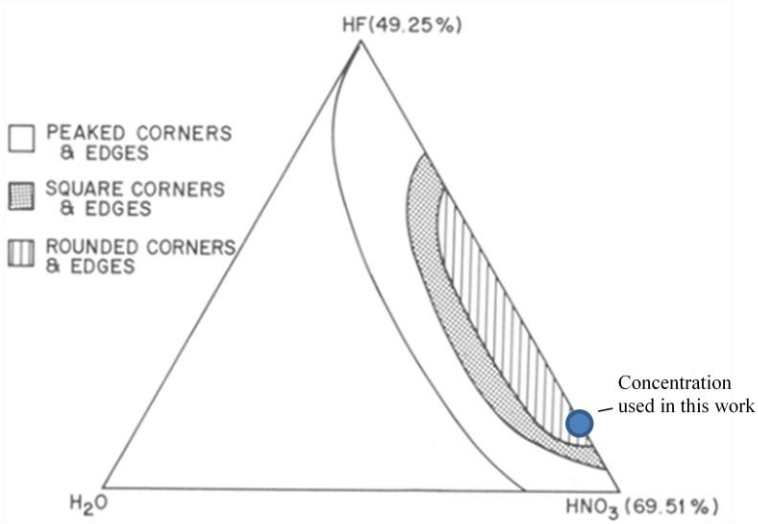

Figure 8. Geometries created from different ratios of hydrofluoric acid and nitric acid. The circle represents the concentration of hydrofluoric acid and nitric acid used in this paper. Image from [16].

To remove the mechanical damage from the sawed wafer pieces, the author developed a polishing etchant of 17% concentrated hydrofluoric acid and 83% concentrated nitric acid. This etch produced a smooth specular surface and rounded the edges of the silicon sample as seen through an optical microscope. It was expected that such smooth, round edges would prevent any local points of high stress that lead to premature sample breakage. Indeed, the polishing etch improved the maximum amount of stress that could be applied to the samples before breaking by over 50% compared to unpolished sawed pieces. The benefits of the polishing etch are shown in Figure 9. The average compressive stress applied to the samples before breakage for the polished pieces was 0.38 GPa while the value for cleaved pieces was 0.31 GPa. The data indicates that all pieces, both cleaved and sawed, may benefit from a polishing etch before being strained.

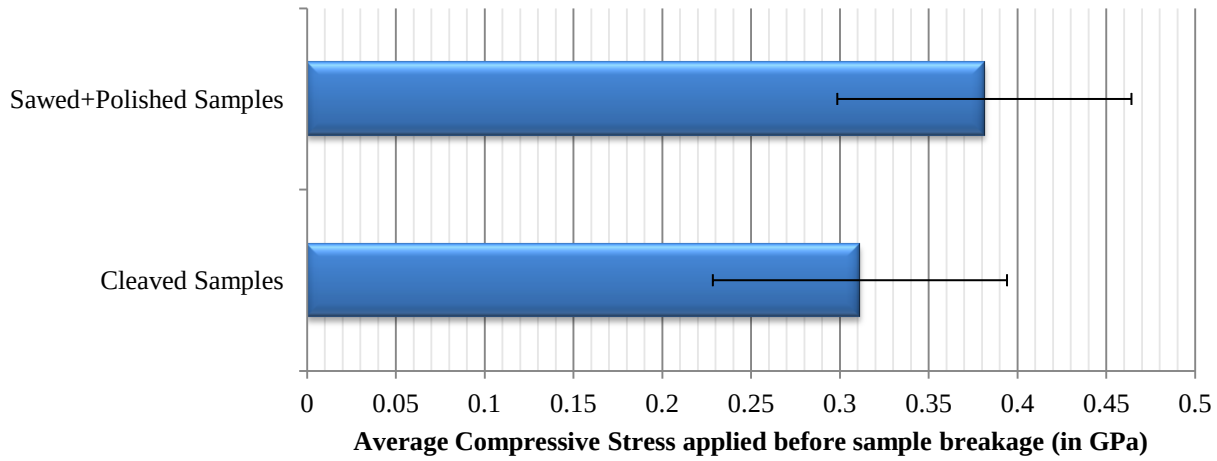

Figure 9. Plot of the average applied compressive strain before breakage for sawed+polished samples and cleaved samples. Error bars indicate standard deviation of the data.

3.5 Bending Apparatus

A flexure jig designed by the Scott Thompson group at the University of Florida was used to mechanically strain the samples. A drawing of the bending apparatus is shown in Figure 10 below.

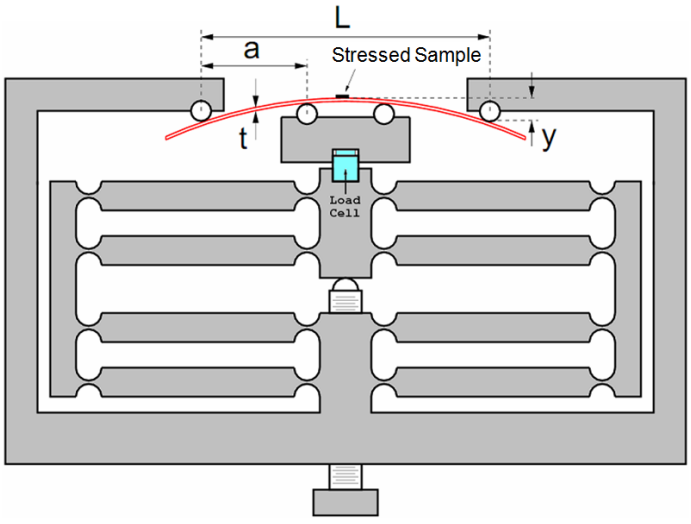

Figure 10. Bending apparatus (not drawn to scale). The load cell shown in the drawing was not implemented. Image from [18].

The 200mm wafers were cut into smaller sample pieces so that they could be loaded into the bending apparatus. A sample size of approximately 1.8 cm x 5.5 cm fit nicely into the apparatus and was easy to handle. The sample contacted four round stainless steel pins when loaded into the bending apparatus. Two pins were placed on the top of the sample, and two pins were placed at the bottom of the sample as seen in Figure 10. Stress was applied to the sample by rotating the nut at the bottom of the apparatus. This raises the stage on which the sample sits causing the sample to bend.

In the configuration pictured, the sample curvature exerts a tensile force on the top surface of the sample piece as the stage is raised. In the opposite configuration, where the pins on the top of the sample are located closer together than the pins on the bottom, a compressive force is exerted. It should be noted that Figure 10 is not drawn to scale. In the actual bending apparatus, the opening above the sample is much smaller, and the stage on which the sample rests is much bigger. From the picture, it looks as though the top pins cannot be moved closer together than the bottom pins. This is not the case in the real apparatus as both compressive and tensile strain can be applied to the samples.

3.5.1 Calibration of the Bending Apparatus

The bending apparatus was calibrated using commercial strain gauges purchased from Omega Engineering, Inc. The model number of the strain gauges was SGT-3F/350-TY11. The strain gauges function on the property that

$$\frac{\Delta R_{gauge}}{R_{gauge}} = GF\frac{\Delta L}{L} \equiv GF \cdot \epsilon \tag{42}$$

where GF is the gauge factor of the strain gauge which is dependent on the material properties of the gauge, R_{gauge} is the resistance of the strain gauge, L is the length of the gauge, and ϵ is the

strain along the length of the strain gauge. The gauge factor for the strain gauges used in this experiment was approximately 2.

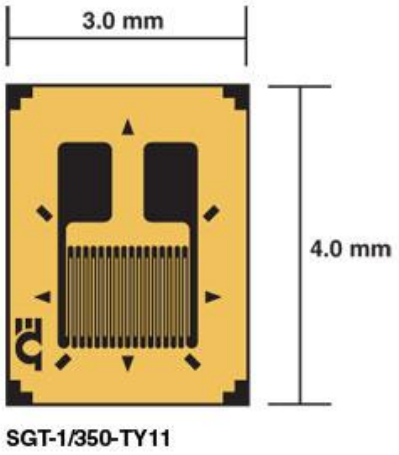

Figure 11. Drawing of a strain gauge used for calibration. Image from [19].

The strain gauges were affixed to the surface of several test pieces using 910 Permabond (ethyl-2-cyanoacrylate adhesive commonly known as super glue) using the procedure listed in Appendix A: *Procedure for Bonding Strain Gauge to* Samples. Stress was applied to the test pieces using the bending apparatus by manually turning a nut located on the bottom of the flexure jig. The underside of the apparatus has a circle that is divided into 24 markings of 15 degrees of rotation each. The alignment marks on the nut allowed determination of the amount of rotation of the nut. At low stresses, the nut was carefully turned by hand while at higher stress, a wrench was used to rotate the nut.

3.5.2 Electrical Measurements of Strain Gauge

To determine the amount of strain applied by rotating the nut, the change in resistance of the strain gauge was measured. An accuracy of 0.01% strain was desired for the strain measurement, which required measuring 10 μV changes in signal. To facilitate the required accuracy, a

Wheatstone bridge was used to measure the change in resistance of the strain gauge as stress was applied. Figure 12 shows a circuit diagram of the Omega model BCM-1 Wheatstone bridge used in the electrical measurements where R_x is the resistance of strain gauge.

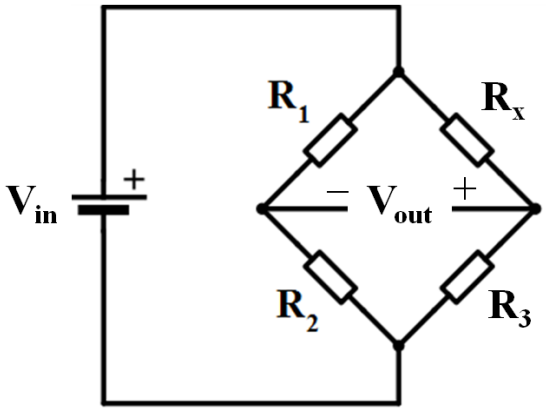

Figure 12. Circuit diagram of the Wheatstone bridge used to measure the change in resistance of the strain gauge. Image from [20].

In the circuit above, V_{out} is given by

$$V_{out} = \left(\frac{R_3}{R_3 + R_x} - \frac{R_2}{R_2 + R_1}\right) V_{in} \tag{43}$$

In the Wheatstone bridge model used in the experiment, all the resistors were nominally 350Ω, and R_3 was adjustable so that $R_3 = R_x$ and $V_{out} = 0$ at zero applied stress. By rearranging the above equation and making the approximation that $\frac{\Delta R_x/2}{2R_x + \Delta R_x} \approx \frac{\Delta R_x}{4R_x}$ for small changes in strain gauge resistance, we find that

$$\frac{\Delta R_x}{R_x} \approx -4\frac{V_{out}}{V_{in}} \tag{44}$$

Plugging this equation into Equation (42), the relation between measured voltage and strain is given by

$$\epsilon = -2\frac{V_{out}}{V_{in}} \tag{45}$$

Measurements were made on several wafer pieces with thicknesses between 720-740µm to correctly determine the amount of strain applied per rotation of the nut of the bending apparatus, and the results are shown in Appendix B: *Calibration Measurements of the Bending Apparatus*. On average, approximately 0.26% strain is applied to the sample per full rotation of the nut for pieces with a thickness of approximately 730µm.

Chapter 4: The Stress/Strain Relation

The tensor form of Hooke's law that relates stress and strain is given by

$$\sigma = \boldsymbol{c}\epsilon \tag{46}$$

where

$$stress = \sigma \equiv \begin{bmatrix} \sigma_{11} & \sigma_{12} & \sigma_{13} \\ & \sigma_{22} & \sigma_{23} \\ sym. & & \sigma_{33} \end{bmatrix} \equiv \begin{bmatrix} \sigma_{xx} & \sigma_{xy} & \sigma_{xz} \\ & \sigma_{yy} & \sigma_{yz} \\ sym. & & \sigma_{zz} \end{bmatrix}, \tag{47}$$

$$strain = \epsilon \equiv \begin{bmatrix} \epsilon_{11} & \epsilon_{12} & \epsilon_{13} \\ & \epsilon_{22} & \epsilon_{23} \\ sym. & & \epsilon_{33} \end{bmatrix} \equiv \begin{bmatrix} \epsilon_{xx} & \epsilon_{xy} & \epsilon_{xz} \\ & \epsilon_{yy} & \epsilon_{yz} \\ sym. & & \epsilon_{zz} \end{bmatrix}, \tag{48}$$

and $\boldsymbol{c}$ is the fourth-rank elastic stiffness matrix of size 3x3x3x3 relating stress and strain. The stress and strain are given by a 3x3 matrices where the notation 1, 2, and 3 represent the *x*, *y*, and *z* coordinate axes aligned with the $[100]$, $[010]$, and $[001]$ crystal axes respectively. The off-diagonal elements of the stress and strain matrices represent shear stresses (i.e. stress applied parallel to the surface of a material) and shear strains. Additionally, the diagonal components of the matrices represent normal stress or strain applied perpendicular to a surface. The matrices only have 6 unique values since they are symmetric ($\sigma_{ij} = \sigma_{ji}$ and $\epsilon_{ij} = \epsilon_{ji}$). Due to this, stress and strain are often rewritten in Voigt notation as a six element column vector, and Equation (46) is rewritten in matrix form as

(matrix form)
$$\begin{bmatrix} \sigma_1 \\ \sigma_2 \\ \sigma_3 \\ \sigma_4 \\ \sigma_5 \\ \sigma_6 \end{bmatrix} = \begin{bmatrix} c_{11} & c_{12} & c_{13} & c_{14} & c_{15} & c_{16} \\ & c_{22} & c_{23} & c_{24} & c_{25} & c_{26} \\ & & c_{33} & c_{34} & c_{35} & c_{36} \\ & & & c_{44} & c_{45} & c_{46} \\ & sym. & & & c_{55} & c_{56} \\ & & & & & c_{66} \end{bmatrix} \cdot \begin{bmatrix} \epsilon_1 \\ \epsilon_2 \\ \epsilon_3 \\ \gamma_4 \\ \gamma_5 \\ \gamma_6 \end{bmatrix} \tag{49}$$

where the mapping from tensor form to matrix form is shown below

$$\begin{bmatrix} \sigma_{11} & \sigma_{12} & \sigma_{13} \\ & \sigma_{22} & \sigma_{23} \\ sym. & & \sigma_{33} \end{bmatrix} \leftrightarrow \begin{bmatrix} \sigma_1 & \sigma_6 & \sigma_5 \\ & \sigma_2 & \sigma_4 \\ sym. & & \sigma_3 \end{bmatrix} \tag{50}$$

(tensor form) (matrix form)

$$\begin{bmatrix} \epsilon_{11} & \epsilon_{12} & \epsilon_{13} \\ & \epsilon_{22} & \epsilon_{23} \\ sym. & & \epsilon_{33} \end{bmatrix} \leftrightarrow \begin{bmatrix} \epsilon_1 & \frac{1}{2}\gamma_6 & \frac{1}{2}\gamma_5 \\ & \epsilon_2 & \frac{1}{2}\gamma_4 \\ sym. & & \epsilon_3 \end{bmatrix} \tag{51}$$

and

$$\begin{aligned} \gamma_4 &= \epsilon_{23} + \epsilon_{32} = 2\epsilon_{23} \\ \gamma_5 &= \epsilon_{13} + \epsilon_{31} = 2\epsilon_{13} \\ \gamma_6 &= \epsilon_{12} + \epsilon_{21} = 2\epsilon_{12} \end{aligned} \tag{52}$$

In the convention used, the normal stresses are $\sigma_1, \sigma_2,$ and σ_3, and shear stresses are $\sigma_4, \sigma_5,$ and σ_6. Strains are defined by the same convention except for factors of two that appear in the conversion from tensor form to matrix form for the off-diagonal elements. γ is the engineering shear strain and is defined in Equation (52). Some references [21] use the average shear strain (where $\epsilon_4 \equiv \frac{1}{2}\epsilon_{23} + \frac{1}{2}\epsilon_{32}$) instead of engineering shear strain, so care must be taken to avoid errors when using equations from different references. A positive value indicates a tensile stress or strain, while a negative value indicates a compressive stress or strain.

The elastic stiffness matrix in the above equations is a symmetric matrix, and it can be further reduced to three independent coefficients due to the cubic symmetry of the silicon lattice [22]. Therefore, the elastic stiffness matrix for materials with a cubic lattice can be simplified to

$$\begin{bmatrix}\sigma_1\\ \sigma_2\\ \sigma_3\\ \sigma_4\\ \sigma_5\\ \sigma_6\end{bmatrix} = \begin{bmatrix}c_{11} & c_{12} & c_{12} & 0 & 0 & 0\\ c_{12} & c_{11} & c_{12} & 0 & 0 & 0\\ c_{12} & c_{12} & c_{11} & 0 & 0 & 0\\ 0 & 0 & 0 & c_{44} & 0 & 0\\ 0 & 0 & 0 & 0 & c_{44} & 0\\ 0 & 0 & 0 & 0 & 0 & c_{44}\end{bmatrix} \cdot \begin{bmatrix}\epsilon_1\\ \epsilon_2\\ \epsilon_3\\ \gamma_4\\ \gamma_5\\ \gamma_6\end{bmatrix} \tag{53}$$

which can be rewritten as

$$\begin{aligned}\begin{bmatrix}\epsilon_1\\ \epsilon_2\\ \epsilon_3\\ \gamma_4\\ \gamma_5\\ \gamma_6\end{bmatrix} &= \begin{bmatrix}c_{11} & c_{12} & c_{12} & 0 & 0 & 0\\ c_{12} & c_{11} & c_{12} & 0 & 0 & 0\\ c_{12} & c_{12} & c_{11} & 0 & 0 & 0\\ 0 & 0 & 0 & c_{44} & 0 & 0\\ 0 & 0 & 0 & 0 & c_{44} & 0\\ 0 & 0 & 0 & 0 & 0 & c_{44}\end{bmatrix}^{-1} \cdot \begin{bmatrix}\sigma_1\\ \sigma_2\\ \sigma_3\\ \sigma_4\\ \sigma_5\\ \sigma_6\end{bmatrix}\\ &= \begin{bmatrix}s_{11} & s_{12} & s_{12} & 0 & 0 & 0\\ s_{12} & s_{11} & s_{12} & 0 & 0 & 0\\ s_{12} & s_{12} & s_{11} & 0 & 0 & 0\\ 0 & 0 & 0 & s_{44} & 0 & 0\\ 0 & 0 & 0 & 0 & s_{44} & 0\\ 0 & 0 & 0 & 0 & 0 & s_{44}\end{bmatrix} \cdot \begin{bmatrix}\sigma_1\\ \sigma_2\\ \sigma_3\\ \sigma_4\\ \sigma_5\\ \sigma_6\end{bmatrix}\end{aligned} \tag{54}$$

where the ***s*** is called the elastic compliance matrix.

4.1 Coordinate Transformation for the Stress/Strain Relation

In the experiment stress is applied along the ⟨100⟩ or ⟨110⟩ direction with all other stresses equal to zero. An example of strain calculated for a stress applied in the ⟨100⟩ direction is given in Appendix C: *Strain Calculation for Stress Applied Along the [100] Crystal* Axis. However, the analysis for the case of ⟨110⟩ directed stress is more complicated and requires matrix transformations. Keep in mind that σ_{xy} is *not* stress applied perpendicular to the *xy*-plane; rather, it is shear strain applied parallel to the *x*-surface in the *y*-direction. The *x*, *y*, and *z* coordinates are shown along the crystal coordinate axes in Figure 13. The primed axes represent a change of coordinates used in the analysis of ⟨110⟩ directed stress.

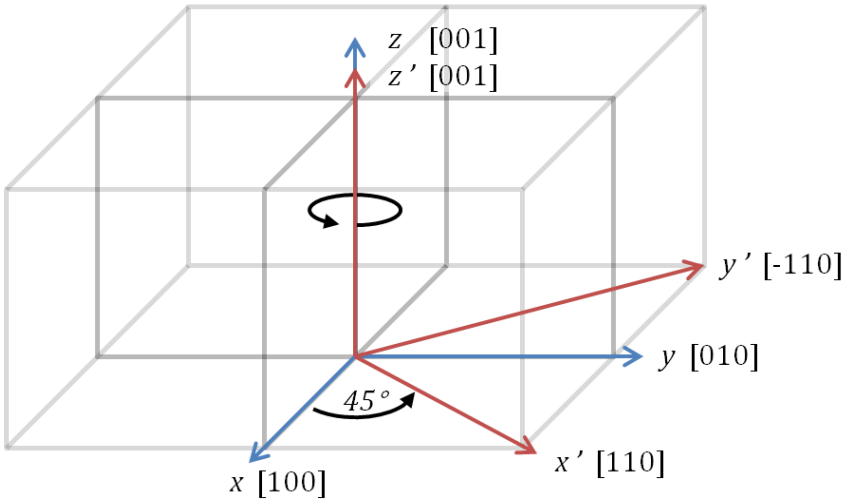

Figure 13. Change of coordinates used in the analysis of <110> stress shown with respect to crystal directions.

The transformation for any second-rank tensor to new coordinate axes is given by

$$T' = aTa^T \tag{55}$$

where

$$a = \begin{bmatrix} a_{11} & a_{12} & a_{13} \\ a_{21} & a_{22} & a_{23} \\ a_{31} & a_{32} & a_{33} \end{bmatrix} \tag{56}$$

and a_{ij} is the direction cosine (or normalized dot product) between x_i' and x_j:

$$a_{ij} = \frac{x_i' \cdot x_j}{|x_i'||x_j|} \tag{57}$$

For example, a_{23} is the cosine of the angle between the y'-coordinate axis and z-coordinate axis (remember: $x_2' \equiv y'$ and $x_3 \equiv z$). Additionally, matrix a is orthogonal so that $a^T = a^{-1}$ is true.

The transformation matrix in vector form becomes quite cumbersome due to the notation of stress and strain as 6x1 column vectors. With some algebra, the transformation matrix for a symmetric second-rank tensor, such as stress, represented in vector notation is found to be

$$\begin{bmatrix}\sigma_1^{'}\\ \sigma_2^{'}\\ \sigma_3^{'}\\ \sigma_4^{'}\\ \sigma_5^{'}\\ \sigma_6^{'}\end{bmatrix} = \left[\begin{array}{ccc:ccc} a_{11}^2 & a_{12}^2 & a_{13}^2 & 2a_{12}a_{13} & 2a_{11}a_{13} & 2a_{11}a_{12} \\ a_{21}^2 & a_{22}^2 & a_{23}^2 & 2a_{22}a_{23} & 2a_{21}a_{23} & 2a_{21}a_{22} \\ a_{31}^2 & a_{32}^2 & a_{33}^2 & 2a_{32}a_{33} & 2a_{31}a_{33} & 2a_{31}a_{32} \\ \hdashline a_{21}a_{31} & a_{22}a_{32} & a_{23}a_{33} & a_{22}a_{33}+a_{23}a_{32} & a_{21}a_{33}+a_{23}a_{31} & a_{21}a_{32}+a_{22}a_{31} \\ a_{11}a_{31} & a_{12}a_{32} & a_{13}a_{33} & a_{12}a_{33}+a_{13}a_{32} & a_{11}a_{33}+a_{13}a_{31} & a_{11}a_{32}+a_{12}a_{31} \\ a_{11}a_{21} & a_{12}a_{22} & a_{13}a_{23} & a_{12}a_{23}+a_{13}a_{22} & a_{11}a_{23}+a_{13}a_{21} & a_{11}a_{22}+a_{12}a_{21} \end{array}\right] \cdot \begin{bmatrix}\sigma_1\\ \sigma_2\\ \sigma_3\\ \sigma_4\\ \sigma_5\\ \sigma_6\end{bmatrix} \quad (58)$$

Furthermore, Equation (58) can be written compactly as

$$\begin{aligned} & \sigma^{'} = \boldsymbol{\alpha}\sigma \\ \Rightarrow \quad & \sigma = \boldsymbol{\alpha}^{-1}\sigma^{'} \end{aligned} \quad (59)$$

However, the transformation matrix for the strain vector defined in Equation (51) differs from the transformation matrix used for stress due to the factors of two that exist in the fourth through sixth elements of the strain column vector. To properly account for this, the transformation of strain is given by

$$\begin{bmatrix}\epsilon_1^{'}\\ \epsilon_2^{'}\\ \epsilon_3^{'}\\ \gamma_4^{'}\\ \gamma_5^{'}\\ \gamma_6^{'}\end{bmatrix} = \left[\begin{array}{ccc:ccc} a_{11}^2 & a_{12}^2 & a_{13}^2 & a_{12}a_{13} & a_{11}a_{13} & a_{11}a_{12} \\ a_{21}^2 & a_{22}^2 & a_{23}^2 & a_{22}a_{23} & a_{21}a_{23} & a_{21}a_{22} \\ a_{31}^2 & a_{32}^2 & a_{33}^2 & a_{32}a_{33} & a_{31}a_{33} & a_{31}a_{32} \\ \hdashline 2a_{21}a_{31} & 2a_{22}a_{32} & 2a_{23}a_{33} & a_{22}a_{33}+a_{23}a_{32} & a_{21}a_{33}+a_{23}a_{31} & a_{21}a_{32}+a_{22}a_{31} \\ 2a_{11}a_{31} & 2a_{12}a_{32} & 2a_{13}a_{33} & a_{12}a_{33}+a_{13}a_{32} & a_{11}a_{33}+a_{13}a_{31} & a_{11}a_{32}+a_{12}a_{31} \\ 2a_{11}a_{21} & 2a_{12}a_{22} & 2a_{13}a_{23} & a_{12}a_{23}+a_{13}a_{22} & a_{11}a_{23}+a_{13}a_{21} & a_{11}a_{22}+a_{12}a_{21} \end{array}\right] \cdot \begin{bmatrix}\epsilon_1\\ \epsilon_2\\ \epsilon_3\\ \gamma_4\\ \gamma_5\\ \gamma_6\end{bmatrix} \quad (60)$$

which is written succinctly as

$$\begin{aligned} & \epsilon^{'} = \boldsymbol{\beta}\epsilon \\ \Rightarrow \quad & \epsilon = \boldsymbol{\beta}^{-1}\epsilon^{'} \end{aligned} \quad (61)$$

The *strain* transformation matrix, $\boldsymbol{\beta}$, is similar to the *stress* transformation matrix, $\boldsymbol{\alpha}$, except that the bottom-left quadrant of $\boldsymbol{\beta}$ is twice the bottom-left quadrant of $\boldsymbol{\alpha}$ and the top-right quadrant of $\boldsymbol{\beta}$ is half the top-right quadrant of $\boldsymbol{\alpha}$. The algebraic expression relating the $\boldsymbol{\beta}$ matrix to the $\boldsymbol{\alpha}$ matrix is found to be

$$\boldsymbol{\beta} = (\boldsymbol{\alpha}^T)^{-1} \tag{62}$$

such that Equation (61) becomes

$$\begin{aligned} & \epsilon' = (\boldsymbol{\alpha}^T)^{-1}\epsilon \\ \Rightarrow \quad & \epsilon = \boldsymbol{\alpha}^T\epsilon' \end{aligned} \tag{63}$$

While this equation looks somewhat complicated, the action of taking the transpose and then the inverse of $\boldsymbol{\alpha}$ results in arithmetic operations described in the paragraph above. This operation properly accounts for the factors of two introduced in Equation (51).

Applying the coordinate transformation to Equation (54) yields

$$\sigma' = \boldsymbol{\alpha}\sigma = \boldsymbol{\alpha c}\epsilon = \boldsymbol{\alpha c \alpha}^T\epsilon' = \boldsymbol{c}'\epsilon' \tag{64}$$

$$\boldsymbol{c}' = \boldsymbol{\alpha c \alpha}^T \tag{65}$$

$$\boldsymbol{s}' = (\boldsymbol{c}')^{-1} = (\boldsymbol{\alpha c \alpha}^T)^{-1} = (\boldsymbol{\alpha}^T)^{-1}\boldsymbol{c}^{-1}\boldsymbol{\alpha}^{-1} = (\boldsymbol{\alpha}^T)^{-1}\boldsymbol{s}\boldsymbol{\alpha}^{-1} \tag{66}$$

$$\Rightarrow \quad \epsilon' = \boldsymbol{s}'\sigma' \tag{67}$$

To complete the analysis for $\langle 110 \rangle$ directed stress, x' is taken to be along the $[110]$ direction, and y' is taken to be along the $[\bar{1}10]$ direction of the crystal as depicted in Figure 13. Stress is applied along x' with all other stresses equal to zero. For this change of coordinates, the stress transformation matrix, $\boldsymbol{\alpha}$, is given by

$$\boldsymbol{\alpha}_{100\rightarrow110} = \begin{bmatrix} 0.5 & 0.5 & 0 & 0 & 0 & 1 \\ 0.5 & 0.5 & 0 & 0 & 0 & -1 \\ 0 & 0 & 1 & 0 & 0 & 0 \\ 0 & 0 & 0 & 0.5\sqrt{2} & -0.5\sqrt{2} & 0 \\ 0 & 0 & 0 & 0.5\sqrt{2} & 0.5\sqrt{2} & 0 \\ -0.5 & 0.5 & 0 & 0 & 0 & 0 \end{bmatrix} \quad (68)$$

Using Equations (65), (66), and (68), the elastic stiffness matrix and the elastic compliance matrix for the new coordinate frame of reference can be calculated. The values of these matrices for silicon are displayed in Table 2 below.

⟨100⟩ oriented coordinate system $\boldsymbol{x} = [\mathbf{100}]$ $\boldsymbol{y} = [\mathbf{010}]$ $\boldsymbol{z} = [\mathbf{001}]$	$\boldsymbol{c} = \begin{bmatrix} 165.7 & 63.9 & 63.9 & 0 & 0 & 0 \\ 63.9 & 165.7 & 63.9 & 0 & 0 & 0 \\ 63.9 & 63.9 & 165.7 & 0 & 0 & 0 \\ 0 & 0 & 0 & 79.6 & 0 & 0 \\ 0 & 0 & 0 & 0 & 79.6 & 0 \\ 0 & 0 & 0 & 0 & 0 & 79.6 \end{bmatrix}$, in GPa
	$\boldsymbol{s} = \begin{bmatrix} 7.68 & -2.14 & -2.14 & 0 & 0 & 0 \\ -2.14 & 7.68 & -2.14 & 0 & 0 & 0 \\ -2.14 & -2.14 & 7.68 & 0 & 0 & 0 \\ 0 & 0 & 0 & 12.6 & 0 & 0 \\ 0 & 0 & 0 & 0 & 12.6 & 0 \\ 0 & 0 & 0 & 0 & 0 & 12.6 \end{bmatrix}$, in $\left(\frac{10^{-12}}{\text{Pa}}\right)$
⟨110⟩ oriented coordinate system $\boldsymbol{x}' = [\mathbf{110}]$ $\boldsymbol{y}' = [\bar{\mathbf{1}}\mathbf{10}]$ $\boldsymbol{z}' = [\mathbf{001}]$	$\boldsymbol{c}' = \begin{bmatrix} 194.4 & 35.2 & 63.9 & 0 & 0 & 0 \\ 35.2 & 194.4 & 63.9 & 0 & 0 & 0 \\ 63.9 & 63.9 & 165.7 & 0 & 0 & 0 \\ 0 & 0 & 0 & 79.6 & 0 & 0 \\ 0 & 0 & 0 & 0 & 79.6 & 0 \\ 0 & 0 & 0 & 0 & 0 & 50.9 \end{bmatrix}$, in GPa
	$\boldsymbol{s}' = \begin{bmatrix} 5.91 & -0.368 & -2.14 & 0 & 0 & 0 \\ -0.368 & 5.91 & -2.14 & 0 & 0 & 0 \\ -2.14 & -2.14 & 7.68 & 0 & 0 & 0 \\ 0 & 0 & 0 & 12.6 & 0 & 0 \\ 0 & 0 & 0 & 0 & 12.6 & 0 \\ 0 & 0 & 0 & 0 & 0 & 19.6 \end{bmatrix}$, in $\left(\frac{10^{-12}}{\text{Pa}}\right)$

Table 2. Elastic compliance matrices for the two coordinate systems pictured in Figure 13. Values for <100> oriented coordinate system are from [23]. Values for <110> oriented coordinate system are calculated using method described in this thesis.

Using these matrices, the calculation of strain for a given stress along the [110] direction is straightforward. An example of a coordinate transformation completed for [110] stress is illustrated in Appendix D: *Coordinate Transformation Calculated for Stress Along the [110] Crystal* Axis.

Chapter 5: Electrical Measurements and Results

After the samples were prepared, current-voltage (IV) measurements were performed on the vertical diodes. Diodes with low excess current and a nearly ideal current-to-voltage slope in forward bias, indicating good junction quality and low trap density, were found, and the IV characteristic for the diode was then measured in both forward and reverse bias under strain at every quarter rotation of the nut of the bending apparatus. Previous calibration has shown that a quarter turn is approximately equal to 0.065% strain applied to the sample in the bending direction. The bending apparatus applies the same amount of *strain* per rotation of the nut for equal thickness sample pieces of any wafer orientation or bending direction within the limits of the approximations made in the linear theory of elasticity; however, the *stress* applied to the sample per rotation of the nut differs for different bending directions because of the anisotropic stiffness matrix for silicon.

For ⟨100⟩ bending, one full rotation of the nut of the bending apparatus creates 0.26% strain, and this translates to roughly 340 MPa of uniaxial stress in the bending direction. For ⟨110⟩ bending, one full rotation also creates 0.26% strain that is approximately equal to 440 MPa of uniaxial stress applied in the bending direction. Less stress is required to bend the wafer along the [100] crystallographic direction compared to the [110] crystallographic direction due to the atomic structure and bond orientation of the crystal; therefore, the effective *Young's modulus* relating stress and strain varies along different directions since the material is not isotropic.

5.1 Current-Voltage Data

Figure 14 below shows the measured current-voltage (IV) plot for a (001) wafer with strain applied in the [110] direction. The specific sample that is plotted received a boron implant of $1.2x10^{14}$ cm^{-2} at 20keV. The plot exhibits backward-diode characteristics that are typical for the diodes measured in this thesis. When a sufficiently large forward bias (a negative voltage applied to the n-region) is applied, a nearly ideal current-voltage slope is seen; for the diode in Figure 14, the slope is 63 mV/decade of current. At smaller forward biases, the diode enters the trap limited regime where current is believed to be dominated by trap-assisted mechanisms. In reverse bias, the bands are aligned to favorably allow band-to-band tunneling.

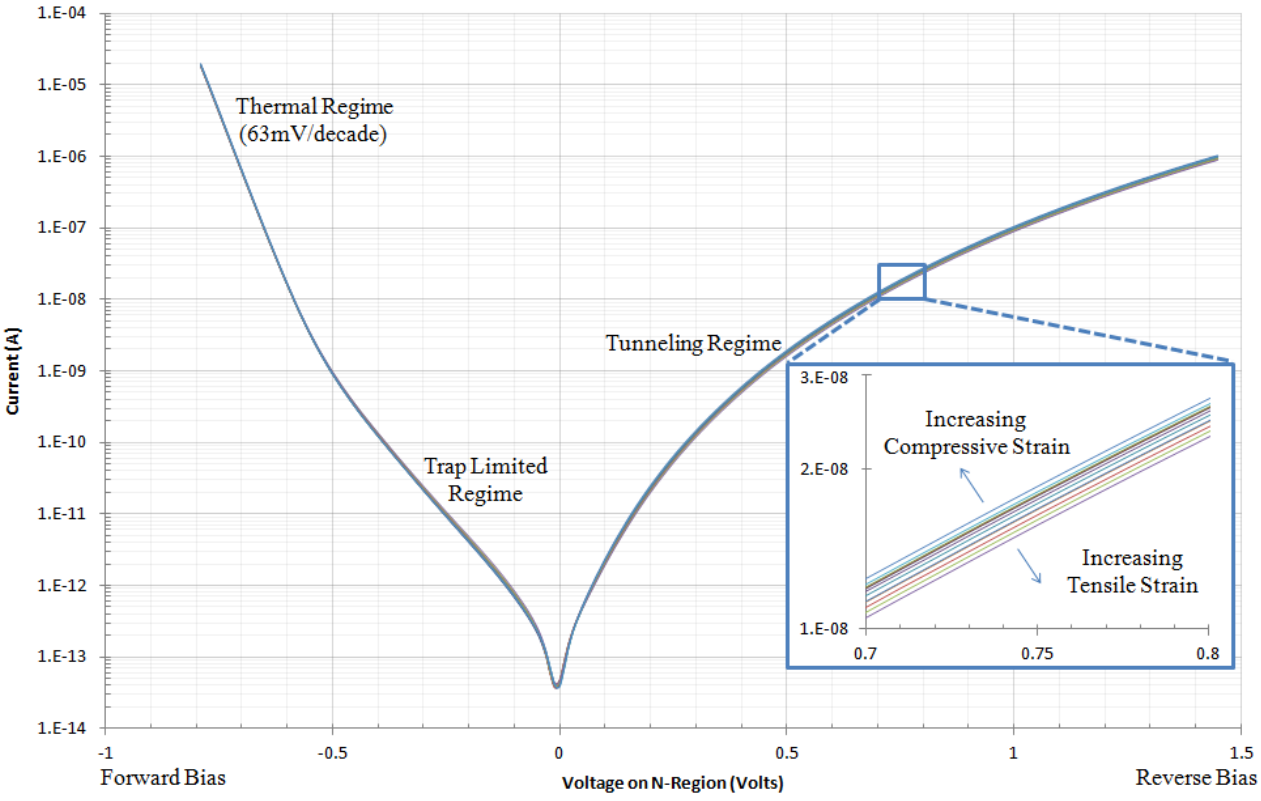

Figure 14. Experimental IV plots for tunneling in the [001] direction for -0.13% to 0.39% strain in the [110] direction. The relative change in the magnitude of current compared to the unstrained case at 0.7 V is quite small for all strains applied: +4.3% change for -0.13% strain and -11.9% change for 0.39% strain.

The inset of Figure 14 is a zoomed in view of the IV curve showing the effect of strain on the measured tunneling currents. For the case pictured, increasing compressive strain resulted in an increase in the magnitude of current while a tensile strain resulted in a decrease. However, the relative change in magnitude of the current is quite small compared with other material parameters that are affected by strain, such as mobility. The relative change in current for reverse bias at different strains is plotted in Figure 15 below.

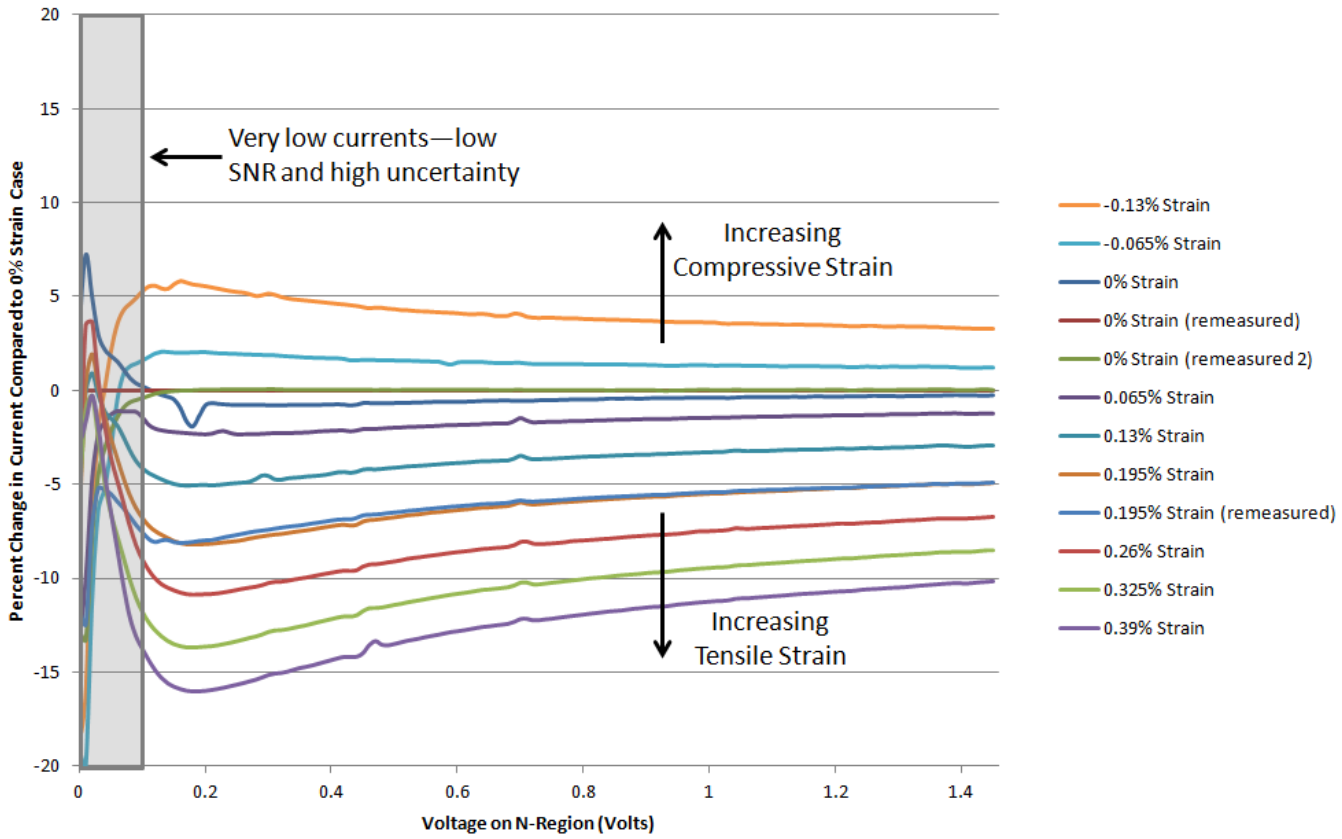

Figure 15. Relative change in current compared to the unstrained case for the experimental IV curve plotted in Figure 14. Tunneling is in the [001] direction. Uniaxial strain of -0.13% to 0.39% was applied along the [110] direction.

As seen in Figure 15, compressive strain resulted in an increase in diode current while tensile strain resulted in a decrease in current for a (001) wafer with strain applied along the

[110] direction. Similar results were also seen for (001) wafers with strain applied along the [100] direction, and (011) wafers with strain applied along the [100] direction. In all three of these wafer/strain configurations, tensile stress decreased the magnitude of current while compressive stress increased the current. However, in the case of $(\bar{1}10)$ wafers with strain applied along the [110] direction, the opposite dependence between strain and change in current was observed, and the data is plotted in Figure 16 below.

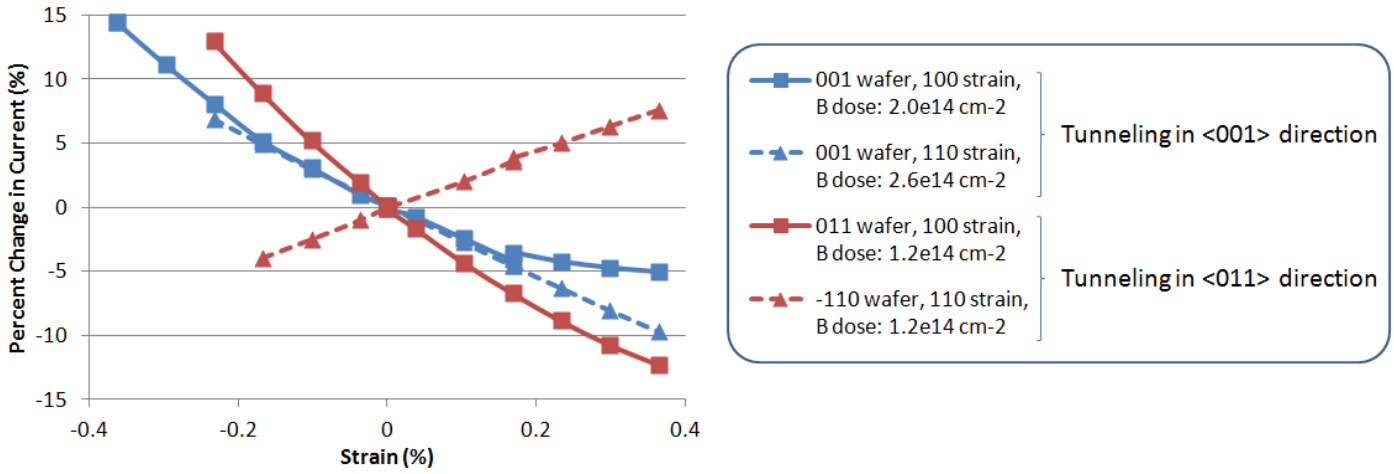

Figure 16. Comparison of the experimental relative change in current versus strain for different wafer/strain configurations and boron doses. The relative change in current is evaluated at a reverse bias of 1 V.

In Figure 17, the change in forward-bias voltage at a constant current around the point of steepest slope is plotted as a function of strain for different wafer/strain configurations. The measured change in voltage is much smaller than the calculated band gap changes with strain. The measurements have a large amount of uncertainty indicated by the error bars. The forward-bias experimental data is presented; however, this thesis does not provide explanation for the observed dependencies.

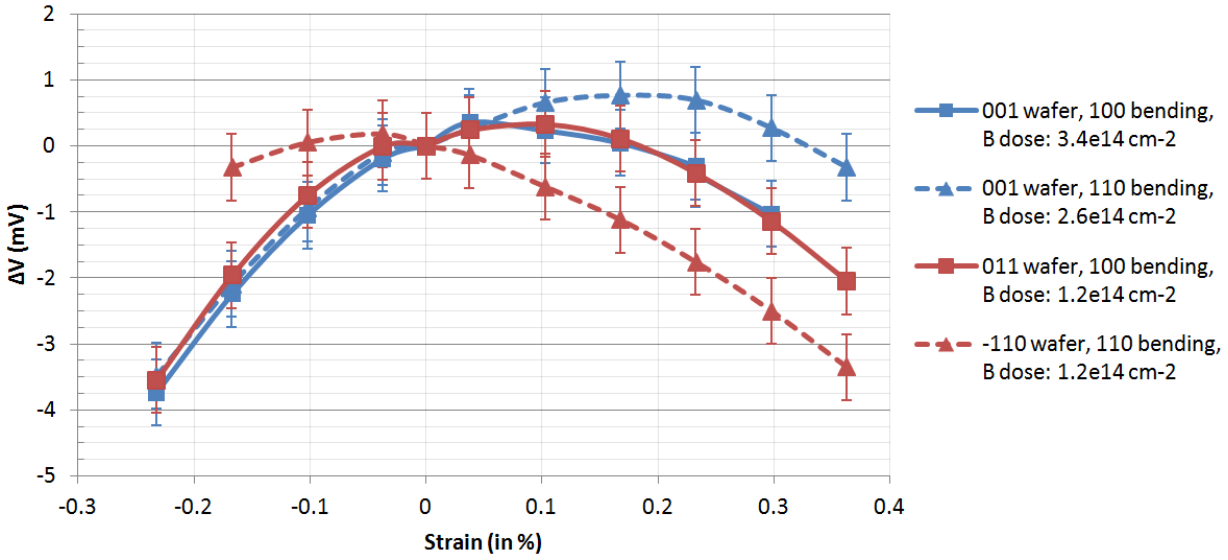

Figure 17. Change in forward-bias voltage at a constant current near the point of steepest slope for different wafer/strain configurations. Changes in voltage are much less than the change in band gap at a given strain. Data points have a considerable uncertainty of ±0.5 mV indicated by error bars.

The theoretical analysis used to explain the different dependencies of reverse bias tunneling current on stress is described in Chapter 6: *Theoretical Current Calculation*.

Chapter 6: Theoretical Current Calculation

The theoretical simulations were performed at MIT in collaboration with Dr. Paul Solomon of IBM. The theoretical calculations for tunneling current consisted of two main parts: the calculation of the change in the band structure due to the applied strain and the calculation of current with the changed band properties.

6.1 Band Structure Strain Analysis

To calculate band structure changes with strain, the *Band Structure Lab* program created by Dr. Mathieu Luisier and others at Purdue's Network for Computational Nanotechnology [10] was used. The *Band Structure Lab* uses the *sp3s*d5* tight-binding method in the calculation of the band structure of silicon. The *sp3s*d5* model uses a 40-band calculation: 10 basis states per atom · 2 spins per state · 2 atoms per lattice site = 40 bands. Shown in Figure 18 are the calculations for the changes in band structure with uniaxial stress applied along the ⟨100⟩ and ⟨110⟩ directions. While the code calculates the full band structure, only the bands of interest are plotted in the figure.

In addition to the *Band Structure Lab*, the *nextnano*^{3} simulation tool [24] was used to calculate the change in the valence bands with applied strain using a 6x6 $k \cdot p$ method, and the Sentaurus Band Structure by Synopsys was used to calculate the conduction bands using an empirical pseudo-potential method [25]. Using multiple programs allowed comparison of simulation results for different methods of band structure calculation. Also, *nextnano*^{3} has the ability to calculate the bulk-3D dispersion for strained cases, which was used to calculate the density-of-states effective mass for the valence band that was dependent on energy due to the

non-parabolicity of the silicon valence bands. A comparison of the band edge calculations using the different programs is shown in Appendix E: *Comparison of Strained Band Structure* .

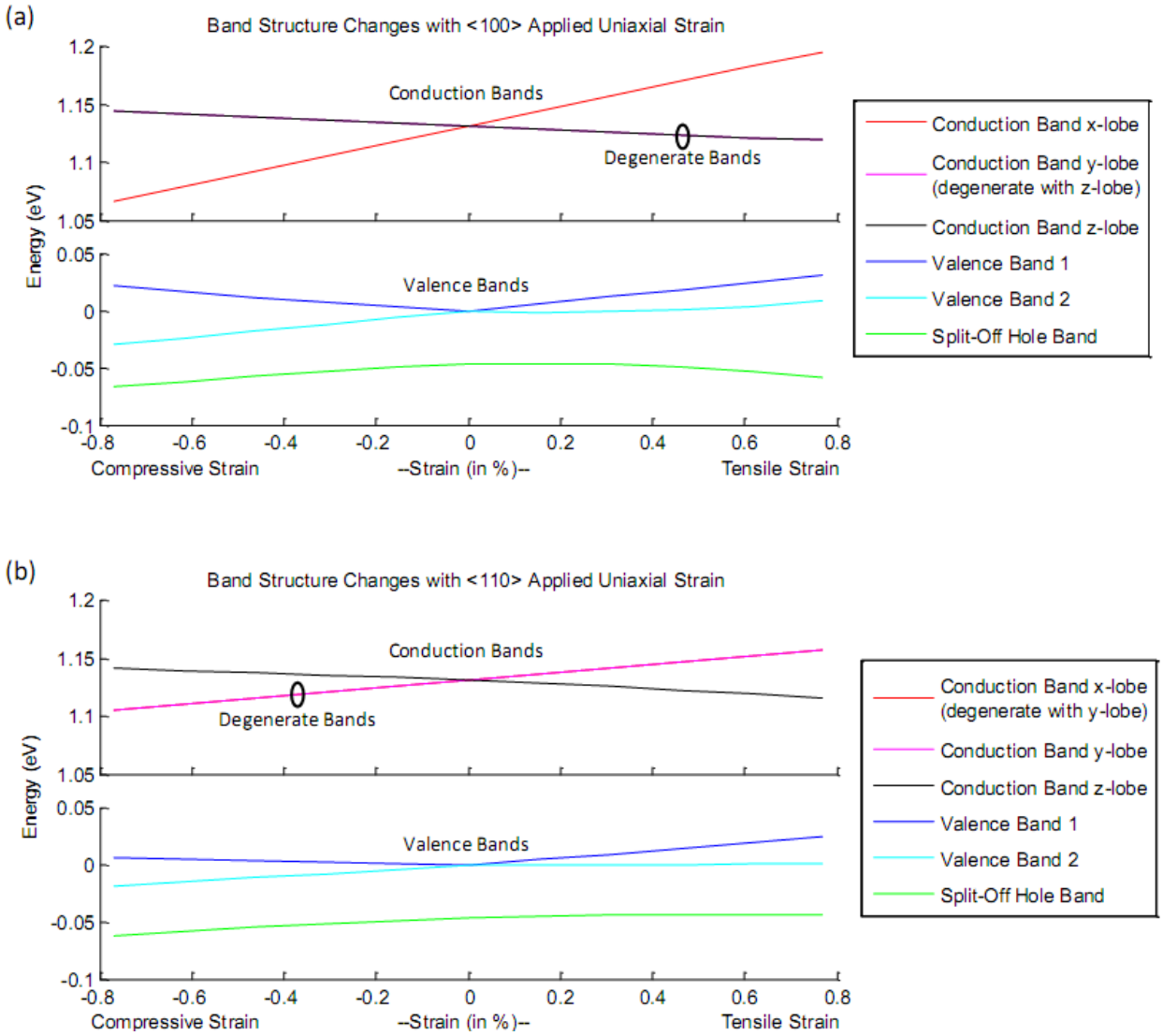

Figure 18. Calculated band structures for bulk silicon using the *Band Structure Lab* [10]. (a) Uniaxial stress is applied along the <100> direction. The energy bands for the *y* and *z* conduction band lobes are identical. (b) Uniaxial stress is applied along the <110> direction. The energy bands for the *x* and *y* conduction band lobes are identical.

The changes in band structure were extracted using the *Band Structure Lab* and then used as inputs for calculating the band-to-band tunneling current as described in the next section. It

was observed that the effective mass of the conduction band valleys changed very little with applied stress so changes in conduction band mass were ignored. This observation is consistent with results seen in literature [26]. Changes in band gap of the three conduction band valleys along with changes in valence band mass are believed to have the strongest impact on the change in tunneling current, and these parameters were used in the calculation of tunneling current.

6.1.1 Valence Band Parameters

Valence band parameters were extracted using the *nextnano*[3] simulation tool. The band edge effective mass used in the tunneling calculation was found by fitting a parabola to the *E-k* data calculated by the program. The *E-k* plot for the valence band with no stress applied is shown in Appendix F: *Valence Band E-k Diagrams*.

The density of states mass was calculated using the 3D $k \cdot p$ dispersion calculated by *nextnano*[3]. Due to the anisotropic valence band of silicon, the density of states mass becomes a function of energy. We start with the typical formula for the density of states:

$$\frac{number\ of\ states}{cm^3} \equiv n = \int g(E)dE = \int \frac{1}{2\pi^2}\left(\frac{2m_{DOS}}{\hbar^2}\right)^{3/2}\sqrt{E}\,dE \tag{69}$$

which implies that

$$\frac{m_{DOS}(E)}{m_0} = \left[\frac{dn}{dE}\left(\frac{2\pi^2}{\sqrt{E}}\right)\right]^{2/3}\frac{\hbar^2}{2m_0} \tag{70}$$

The energy dependent density of states mass was determined for the cumulative valence bands at every applied strain that was simulated.

6.1.2 Conduction Band Parameters

The conduction band mass in the tunneling direction, m_{cx}, is defined as the effective mass along the ellipsoidal conduction band minima. For tunneling in the [100] direction, the tunneling mass for the *y* and *z* conduction band lobes is the transverse mass, $m_t = 0.19m_0$ while the tunneling mass for the *x*-lobe is the longitudinal mass, $m_l = 0.98m_0$ (values from reference [9]).

The tunneling masses for the conduction band in the different crystallographic directions are explained below. We make the approximation that only the relative energy of the conduction band lobes to the valence band are affected by strain and that the effective masses remain constant. The equation for an isoenergy surface for conduction band minima in the *x*-direction is given by

$$E = \frac{\hbar^2}{2}\left[\frac{(k_x - k_{x0})^2}{m_l} + \frac{k_y^2}{m_t} + \frac{k_z^2}{m_t}\right] \tag{71}$$

The effective mass is defined as

$$m^* \equiv \hbar^2 \left(\frac{d^2E}{dk^2}\right)^{-1} \tag{72}$$

so that the effective masses along different directions are

$$\begin{aligned} &x\text{-direction:} && m^*_{100} = \hbar^2\left(\frac{d^2E}{dk^2_{100}}\right)^{-1} = \hbar^2\left(\frac{d^2E}{dk_x^2}\right)^{-1} = m_l \\ &y \text{ and } z\text{-direction:} && m^*_{010} = m^*_{001} = m_t \end{aligned} \tag{73}$$

To find the effective mass in the [110] direction, we use the change of coordinates given below:

$$
\begin{aligned}
k_{x'} &= \frac{\sqrt{2}}{2}k_x - \frac{\sqrt{2}}{2}k_y \\
k_{y'} &= \frac{\sqrt{2}}{2}k_x + \frac{\sqrt{2}}{2}k_y \\
k_{z'} &= k_z
\end{aligned}
\tag{74}
$$

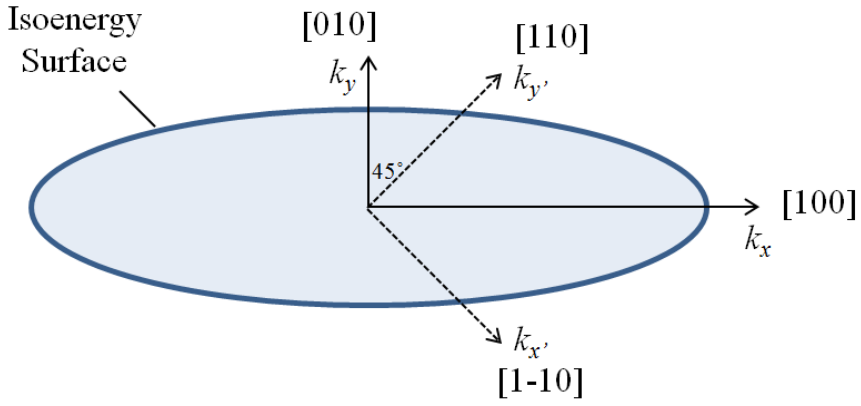

Figure 19. Change of coordinates used for calculating effective mass along the [110] direction of the *x*-directed conduction band lobe.

The equation for energy in terms of the new coordinate system is rewritten as

$$
E = \frac{\hbar^2}{2}\left[\frac{\left(\frac{k_{x'} + k_{y'}}{\sqrt{2}} - k_{x0}\right)^2}{m_l} + \frac{\left(\frac{-k_{x'} + k_{y'}}{\sqrt{2}}\right)^2}{m_t} + \frac{k_{z'}^2}{m_t}\right] \tag{75}
$$

With some algebra, it can be seen that the effective mass along the [110] direction for the *x*-lobe is found to be

$$
m_{110}^* = \hbar^2\left(\frac{d^2E}{dk_{110}^2}\right)^{-1} = \hbar^2\left(\frac{d^2E}{dk_{y'}^2}\right)^{-1} = \frac{2m_l m_t}{m_l + m_t} \tag{76}
$$

A similar analysis can be carried out for all the conduction band lobes.

6.2 Poisson Equation Solution

To determine the tunneling current, the energy band diagram as a function of position in the device must be determined. However, conventional Poisson solvers only include one valence band edge and one conduction band edge. Due to the limitations with available software, a full-band Poisson solver that included the effects of the *x*, *y*, and *z* conduction band minima and the heavy hole, light hole, and split-off hole valence bands was created as part of this work. It is important to include the effects of the individual bands because strain causes band splitting which separates the band extrema and alters effective masses.

The doping profile used as an input to the Poisson solver was found by Solomon using CV techniques combined with SIMS data and TSUPREM calculations. The CV analysis of the diode provided information on the doping profile near the junction. The technique is explained in detail in reference [15]. A plot of the net doping concentration is shown in Figure 20 below.

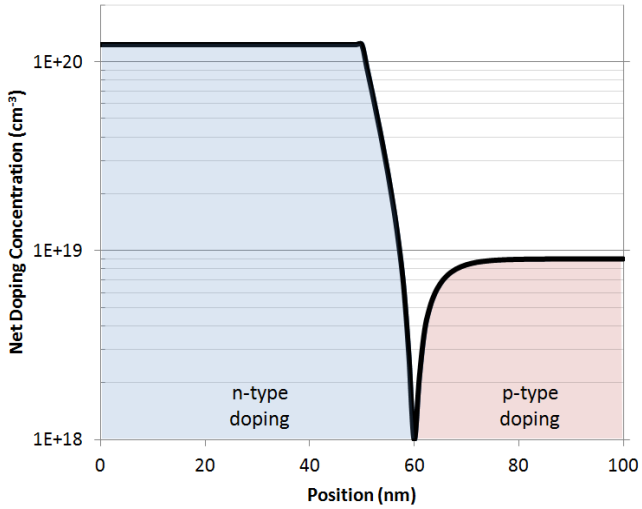

Figure 20. Net doping concentration used as input for the full-band Poisson solver. At 60 nm, the net doping changes from n-type to p-type.

The 1D full-band Poisson solver was not coupled with the continuity equations for current so approximations were made in calculating the band diagram as a function of position. Current was assumed to be negligible in reverse-bias so that the quasi-Fermi levels were approximated as constant throughout the device. Under this approximation, an applied reverse-bias separated the hole quasi-Fermi level and the electron quasi-Fermi level by an amount equal to the applied bias as shown in Figure 21 below.

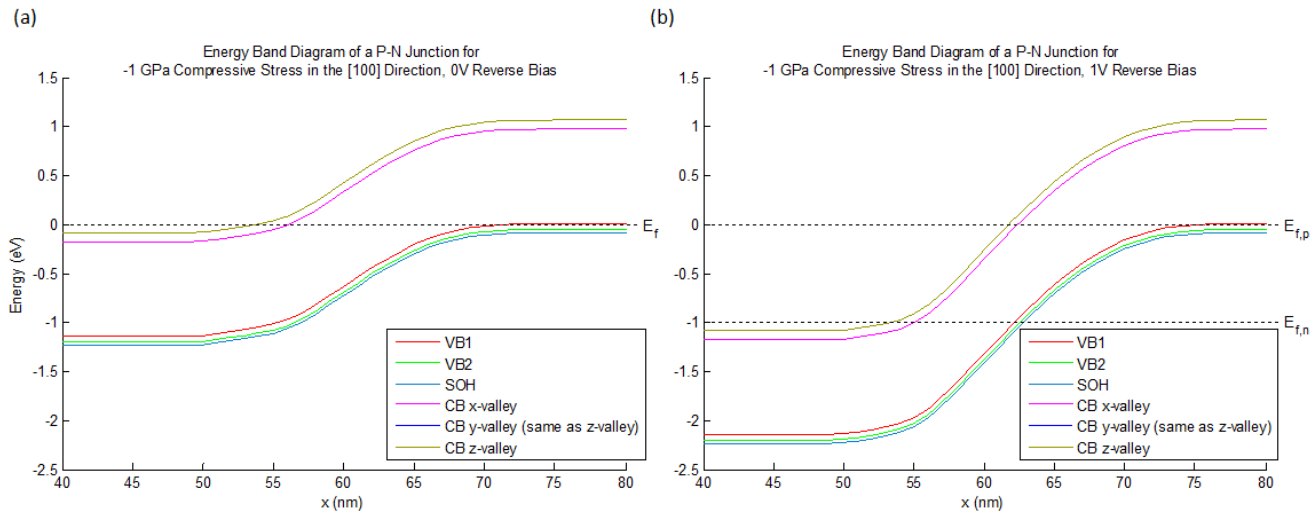

Figure 21. Energy band diagram calculated by full-band Poisson solver for a p-n junction under -1 GPa compressive stress in the [100] direction. (a) Band diagram with 0 V across the junction. (b) Band diagram with 1 V reverse-bias applied across the junction. Current is assumed to be small so quasi-Fermi levels remain constant throughout the device. Both plots show the splitting of the energy bands due to uniaxial strain.

6.3 Equations for Current Flux

The band-to-band current density is derived below using [14] as a reference. The current density from the valence band to conduction band is given by

$$J_{v\to c} = 2q \int \frac{d^3k}{(2\pi)^3} v_x(k_{vx}) T(k_{vx}) f_v(E) \tag{77}$$

In this equation, $v_x(k_{vx})$ is the velocity of a particle with momentum k_{vx} in the tunneling direction, $T(k_{vx})$ is the transmission coefficient, and $f_v(E)$ is the Fermi-Dirac function for the valence band. The prefactor of 2 accounts for particles of both spin states, and $(2\pi)^3$ is the volume of a single *k*-state when length is normalized to 1. Likewise, a similar expression can be written for current density from the conduction band to the valence band:

$$J_{c\to v} = 2q \int \frac{d^3k}{(2\pi)^3} v_x(k_{cx}) T(k_{cx}) f_c(E) \tag{78}$$

At a constant total energy, E, we find that

$$E = E_{v0} - \frac{\hbar^2 k_{vx}^2}{2m_v} - E_\perp = E_{c0} + \frac{\hbar^2 k_{cx}^2}{2m_c} + E_\perp \tag{79}$$

and

$$\begin{aligned} v(k_{vx}) &= \frac{1}{\hbar}\frac{\partial E}{\partial k_{vx}} \;\Rightarrow\; v(k_{vx})\partial k_{vx} = \frac{\partial E}{\hbar} = \frac{\partial E_x}{\hbar} \\ v(k_{cx}) &= \frac{1}{\hbar}\frac{\partial E}{\partial k_{cx}} \;\Rightarrow\; v(k_{cx})\partial k_{cx} = \frac{\partial E}{\hbar} = \frac{\partial E_x}{\hbar} \end{aligned} \tag{80}$$

Combining Equations (77) and (80), current density from the valence band to the conduction band can be written as

$$J_{v\to c} = \frac{q}{\pi\hbar} \int \frac{d^2k_\perp}{(2\pi)^2} \int dE_x T(E_{v\perp}) f_v(E_x + E_\perp) \tag{81}$$

The two-dimensional integral over perpendicular states can be converted to a one-dimensional integral over perpendicular energy using the density of states for a 2D parabolic system:

$$J_{v\to c} = \frac{q}{\pi\hbar} \frac{m_{v_\perp}^*}{2\pi\hbar^2} \int dE_\perp \int dE_x T(E_{v\perp}) f_v(E_x + E_\perp) \tag{82}$$

Therefore, the net current density is given by

$$J_{net} = J_{v\to c} - J_{c\to v} = \frac{qm_{\perp}^{*}}{2\pi^2\hbar^3}\int dE_{\perp}\int T(E_{v\perp})[f_v(E) - f_c(E)]dE \tag{83}$$

Appropriate limits are added to the integrals of Equation (83) :

$$J_{net} = \frac{qm_{\perp}^{*}}{2\pi^2\hbar^3}\int_0^{min\left(E_{v0,p}-E,E-E_{c0,n}\right)} dE_{\perp}\int_{E_{c0,n}}^{E_{v0,p}} T(E_{v\perp})[f_v(E) - f_c(E)]dE \tag{84}$$

$E_{v0,p}$ and $E_{c0,n}$ are depicted in Figure 3. The upper limit of the integral over perpendicular energy arises due to conservation of perpendicular momentum which is explained in Section 2.2. Substituting in Equation (34) for $T(E_x, k_{v\perp}, k_{c\perp})$ in the above equation gives an equation for current that can be solved:

$$J_{net} = \frac{qm_{\perp}^{*}}{2\pi^2\hbar^3}\int_{E_{c0,n}}^{E_{v0,p}} T(E)[f_v(E) - f_c(E)]dE \tag{85}$$

where

$$\begin{aligned} T(E) &= \int_0^{E_{\perp,max}=min\left(E_{v0,p}-E,E-E_{c0,n}\right)} T(E_{v\perp})dE_{\perp} \\ &= -\frac{q|F|\hbar}{(E_G)^{0.5}\sqrt{2m_r}}\left(\frac{m_{v\perp}}{m_r}\right)^{-1} exp\left[-\frac{4}{3}\frac{(E_G)^{1.5}}{q|F|\hbar}\sqrt{2m_r}\right] \\ &\qquad \cdot exp\left[-2\left(\frac{(E_G)^{0.5}}{q|F|\hbar}\sqrt{2m_r}\frac{m_{v\perp}}{m_r}E_{v\perp}\right)\right]_0^{E_{\perp,max}=min\left(E_{v0,p}-E,E-E_{c0,n}\right)} \\ &= \frac{q|F|\hbar}{(E_G)^{0.5}\sqrt{2m_r}}\left(\frac{m_{v\perp}}{m_r}\right)^{-1} exp\left[-\frac{4}{3}\frac{(E_G)^{1.5}}{q|F|\hbar}\sqrt{2m_r}\right] \\ &\qquad \cdot\left(1 - exp\left[-2\left(\frac{(E_G)^{0.5}}{q|F|\hbar}\sqrt{2m_r}\left(\frac{m_{v\perp}}{m_r}\right)E_{v\perp,max}\right)\right]\right) \end{aligned} \tag{86}$$

The current is carried by electrons, and this leads to a final expression for current as a function of energy:

$$J_{net} = \frac{-em_{\perp}^{*}}{2\pi^{2}\hbar^{3}} \int_{E_{c0,n}}^{E_{v0,p}} T(E)[f_v(E) - f_c(E)]dE \tag{87}$$

6.4 Theoretical Calculation of the Relative Change in Current

The previous section serves as the framework for the calculation of band-to-band tunneling current of tunnel diodes in reverse bias. Equation (87) gives the current from the valence band to the conduction band; however, this current must be calculated for all the valence bands to all the conduction bands resulting in 9 components of current:

$$\begin{aligned} J_{total} = {} & J_{VB1\to x} + J_{VB1\to y} + J_{VB1\to z} + J_{VB2\to x} + J_{VB2\to y} + J_{VB2\to z} \\ & + J_{SOH\to x} + J_{SOH\to y} + J_{SO\to z} \end{aligned} \tag{88}$$

The relative change is then easily calculated once the total current densities are known.

The electric field used in Equation (86) is approximated as the maximum field across the junction. The valence band mass in the tunneling direction, m_{vx}, was calculated by fitting a parabola along the tunneling direction to the band structure data calculated by *nextnano*[3] as described in Section 6.1.1. A similar method was used to calculate valence band masses in the perpendicular direction. Likewise, the conduction band masses in the tunneling and perpendicular directions were calculated assuming ellipsoidal conduction band valleys using the method described in Section 6.1.2.

The band gap used in the calculation of the transmission probability in Equation (86) is determined by the difference in energy between the specific conduction band and the valence band for which tunneling is being considered. The band gap is no longer identical for all the different conduction bands when strain is applied since strain splits the bands.

The results of the theoretical simulations are compared with the experimental results below:

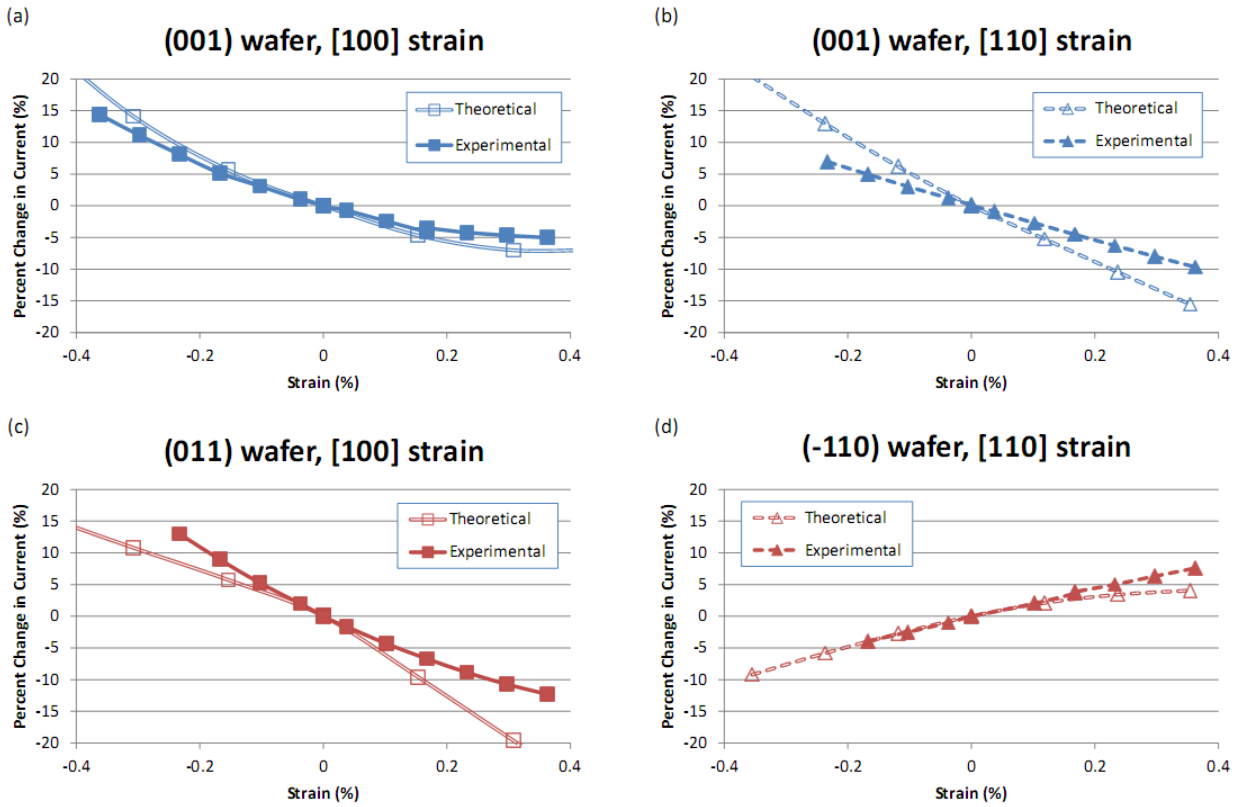

Figure 22. Comparison of theoretically calculated and experimentally measured relative change in current at 1 V reverse bias. (a) Strain applied in [100] direction for [001] tunneling. (b) Strain applied in [110] direction for [001] tunneling. (c) Strain applied in [100] direction for [011] tunneling. (d) Strain applied in [110] direction for [-110] tunneling.

As seen in Figure 22, the theoretical calculations generally match the behavior of experimental results. In cases (a), (b), and (c), the magnitude of tunneling current decreases with increasing strain; however in case (d), increasing uniaxial strain causes an increase in current.

The changes in current can be qualitatively interpreted by referring to change in band structure with strain shown in Figure 18. Below, a quick calculation is outlined to provide insight into the behavior of the results. For case (a), consider only tunneling from the top valence

band to the *x* and *y*-conduction band lobes since the tunneling mass is large in the *z*-direction, and assume that the change in band gap from the *x*-lobe to the top valence band and from the *y*-lobe to the top valence band is linear with strain. The equation for the band gap can be written as

$$E_{G_{VB1\to x}} \approx E_{G0} + s_x\epsilon_{xx} = 1.13 + 0.0848\epsilon_{xx}$$
$$E_{G_{VB1\to y}} \approx E_{G0} + s_y\epsilon_{xx} = 1.13 - 0.0165\epsilon_{xx} \quad (89)$$

(where ϵ_{xx} is in percent)

For the purpose of determining the qualitative behavior of the change in current with strain, we make the assumption that tunneling current is directly proportional to the transmission probability at some arbitrary energy. To simplify the analysis, only the change in the exponential term of the tunneling current with strain is included. This approximation is justified for the cases described in this thesis where the field is relatively small and the exponential term is large. With this assumption we find that

$$J_{total} = J_{VB1\to x} + J_{VB1\to y} \propto T_{VB1\to x} + T_{VB1\to y} \quad (90)$$

$$T_{VB1\to x} = exp\left[-r\left(E_{G_{VB1\to x}}\right)^{1.5}\right] = exp\left[-r(E_{G0})^{1.5}\left(1 + \frac{s_x}{E_{G0}}\epsilon_{xx}\right)^{1.5}\right] \quad (91)$$

where

$$r = \frac{4}{3}\frac{1}{q|F|\hbar}\sqrt{2m_r} \quad (92)$$

Since $\frac{s_x}{E_{G0}}$ is very small, we approximate $\left(1 + \frac{s_x}{E_{G0}}\epsilon_{xx}\right)^{1.5} \approx \left(1 + 1.5\frac{s_x}{E_{G0}}\epsilon_{xx}\right)$ for ϵ_{xx} near zero using Taylor's theorem to the first-order. With this approximation, Equation (91) can be rewritten as

$$T_{VB1\to x} = exp[-r(E_{G0})^{1.5}]\, exp\left[-r(E_{G0})^{1.5}\left(1.5\frac{s_x}{E_{G0}}\epsilon_{xx}\right)\right] \tag{93}$$

so that

$$J_{total} \propto exp[-r(E_{G0})^{1.5}]\left(exp\left[-r(E_{G0})^{1.5}\left(1.5\frac{s_x}{E_{G0}}\epsilon_{xx}\right)\right] + exp\left[-r(E_{G0})^{1.5}\left(1.5\frac{s_y}{E_{G0}}\epsilon_{xx}\right)\right]\right) \tag{94}$$

Lastly, we apply the Taylor series approximation for e^x centered on zero:

$$\begin{aligned} J_{total} &\propto exp[-r(E_{G0})^{1.5}]\left(2 - 1.5\cdot r(E_{G0})^{0.5}(s_x + s_y)\epsilon_{xx}\right) \\ J_{total} &\propto (2 - 1.5\cdot r'(0.0848 - 0.0165)\epsilon_{xx}) \\ &= (2 - 0.10245 r'\epsilon_{xx}) \end{aligned} \tag{95}$$

where

$$r' = r(E_{G0})^{0.5} \tag{96}$$

For case (a), we find that compressive strain applied in the [100] direction results in an increase in current while tensile strain results in a decrease in current, which is seen in Figure 22a. The results stem from the change in band gap with strain of the *x* and *y*-lobes as tunneling to the *z*-lobe is inhibited due to its large longitudinal tunneling mass. Since uniaxial stress is applied along the [100] crystal direction, more strain exists along the *x*-direction compared to the *y*-direction due to Poisson's ratio, and the *x*-lobe dominates the behavior of the change in current at low stresses.

These equations are only valid for qualitative analysis near zero strain. At higher tensile strains, the band gap between the *y*-lobe and the top valence band becomes increasingly small so that current no longer decreases with large tensile strains (seen around 0.4% strain in Figure 22a). At even larger tensile strains (strains greater than 0.5% that were not achieved experimentally), the theoretical calculations predict that current will increase as the band gap

between the *y*-lobe and the top valence band shrinks and the transmission probability increases exponentially allowing more current to flow.

The relative change in current seen in case (d) can be explained easily if the majority of tunneling is considered to occur between the top valence band and *z*-conduction band lobe. This is a reasonable assumption because the mass in the $[\bar{1}10]$ tunneling direction for the *z*-conduction band lobe is significantly smaller than the mass in the $[\bar{1}10]$ tunneling direction for the *x* and *y*-lobes found in Equation (76). Since the band gap between the *z*-lobe and top valence band decreases with increasing tensile strain in the $[110]$ direction as shown in Figure 18b, current increases as positive strain is applied. This explains the opposite dependence on strain for case (d) as compared the other cases depicted.

6.4.1 Simplified Physical Analysis

A simplified equation for tunneling current is used to allow for a concise physical explanation of the effect of strain for the different wafer/strain orientations:

Simplified Approximation:

$$J \propto T \approx exp\left[-\frac{4}{3}\frac{(E_G)^{1.5}}{q|F|\hbar}\sqrt{2m_{tunnel}}\right] \tag{97}$$

This simplified equation shows that the current decreases exponentially with the square root of the tunneling mass. To first order, only conduction band lobes with a small mass in the tunneling direction significantly contribute to the tunneling current. This statement is used as the basis for the analysis of the change in current with strain in the next sections.

6.4.1.1 Stress Applied Along the [100] Direction

For *z*-directed $[001]$ tunneling, the tunneling mass is equal to the transverse mass for the *x* and *y*-lobes and the longitudinal mass for the *z*-lobe as shown in Figure 23. The *z*-lobe is ignored due to

its large tunneling mass. The net change in current is believed to be dominated by the behavior of the *x*-lobe since the energy minimum of the *x*-lobe changes with stress about five times as fast as the energy minimum of the *y*-lobe for stress applied in the [100] direction. With these approximations, the relative change in current only depends on the changes of the *x*-lobe. Since the *x*-lobe energy decreases for compressive stress, an increase in tunneling current is seen, and the opposite effect is seen for tensile stress resulting in a decrease in current.

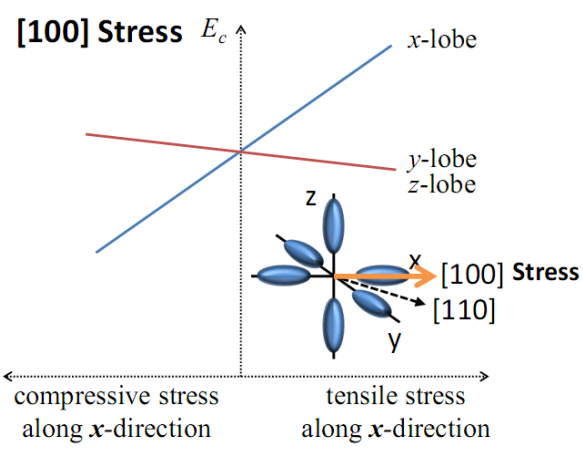

	[001] tunneling	[011] tunneling
x-lobe	m_t=0.19	m_t=0.19
y-lobe	m_t=0.19	m_{mixed}=0.32
z-lobe	m_l=0.98	m_{mixed}=0.32
	$J \approx J_x + J_y$ $\frac{\Delta J}{J} \approx \frac{\Delta J_x + \Delta J_y}{J_{x0} + J_{y0}}$	$J \approx J_x$

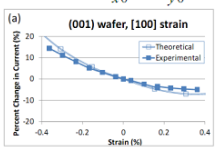

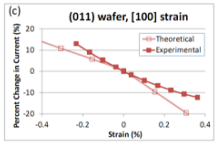

Figure 23. Diagram illustrating the dependence of tunneling current with [100] stress. The left plot shows the change in the conduction band energy for the different lobes with stress. The right table lists the tunneling masses for the conduction band lobes and the approximate equation for current based on the contributing bands. The plots below the table are reproduced from Figure 22 to show the strain dependence of current.

A similar analysis is used to explain the change in current for [011] tunneling with [100] applied stress. In this case, the *x*-conduction band lobe is the only lobe with a transverse mass in the tunneling direction. The *y* and *z*-lobes have a mixed mass in the tunneling direction, explained in Section 6.1.2. Continuing with the simplified analysis, only the *x*-lobe significantly contributes to the current so that the same trend for [001] tunneling is seen for [011] tunneling with stress applied along the [100] direction.

6.4.1.2 *Stress Applied Along the [110] Direction*

Following the work of Section 6.4.1.1, a simplified analysis is carried out to explain the dependencies seen in the relative change in current for stress applied in the [110] direction. The *x* and *y*-lobes have a transverse mass for tunneling in the [001] direction. The energy minimum of the *x* and *y*-lobes is degenerate for stress applied along the [110] direction as shown in Figure 24. Therefore, the current increases for compressive stress and decreases for tensile stress.

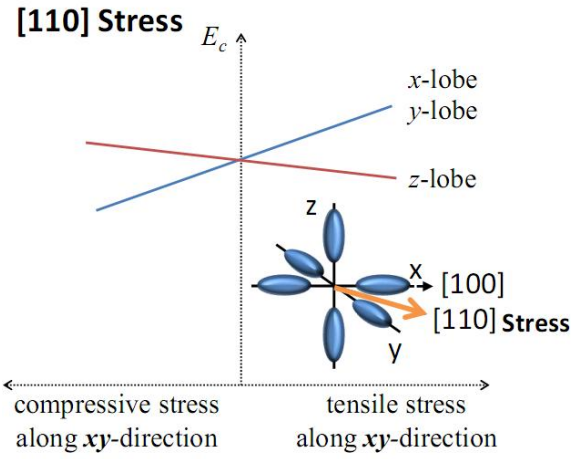

	[001] tunneling	[-110] tunneling
x-lobe	m_t=0.19	m_{mixed}=0.32
y-lobe	m_t=0.19	m_{mixed}=0.32
z-lobe	m_l=0.98	m_t=0.19
	$J \approx J_x + J_y$	$J \approx J_z$

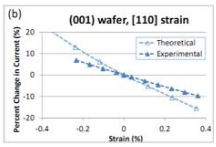

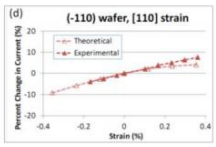

Figure 24. Diagram illustrating the dependence of tunneling current with [110] stress. The left plot shows the change in the conduction band energy for the different lobes with stress. The right table lists the tunneling masses for the conduction band lobes and the approximate equation for current based on the contributing bands. The plots below the table are reproduced from Figure 22 to show the strain dependence of current.

Only the *z*-lobe has a transverse mass in the $[\bar{1}10]$ tunneling direction so the small contribution of the *x* and *y*-lobes to the total current is ignored. Under these approximations, current is seen to decrease due to the increase in the *z*-lobe energy with compressive stress. Conversely, the *z*-lobe energy minimum decreases with tensile stress resulting in an increase in current as shown in Figure 24. These approximations allow for intuitive analyses that explain the effect of stress on tunneling current for various wafer/strain configurations.

6.4.2 Sources of Error in Theoretical Calculation

The direct tunneling equation is used to calculate the transmission probability. This equation forces the momentum of the particle in the valence band to be identical to the momentum of the particle on the conduction band after tunneling since no phonon interaction occurs. This treatment is used to simplify the analysis so that phonon interaction does not have to be considered, but also introduces error from both the neglecting of phonon-interaction and requirement of equal perpendicular momentum.

The electric field used in Equation (86) has a moderate uncertainty that can introduce errors in the theoretical calculation of current, since the transmission probability depends exponentially on the electric-field of the junction. CV analysis was conducted by Solomon et. al [5] to determine the doping profile of the junction; however, this method is unable to reliably reproduce the *exact* doping profile in the device. The field is calculated from the full-band Poisson solver using a doping profile as an input, and therefore the uncertainty in the doping profile introduces error into the theoretical data. Moreover, the electric field was assumed to be constant throughout the junction, which is not the case in the real device.

The effects of heavy-doping, such as band gap narrowing, were not accounted for in the calculation of the band structure of the diodes. Additionally, the theoretical equations for tunneling current use an effective tunneling mass equal to the band-edge mass in the tunneling direction. While this parabolic band-edge mass is commonly used as the tunneling mass, Laux has shown that the parabolic approximation is inadequate to represent the complex band structure of silicon [27]. Work is in progress to include complex band structure with strain in the analysis of tunneling current.

Chapter 7: Summary

This thesis details the effect of mechanical uniaxial strain on band-to-band tunneling in silicon diodes. In Chapter 2: *Introduction to Quantum Tunneling*, the topic of quantum tunneling is introduced, and the specific case of band-to-band tunneling in diodes is explained. The transmission coefficients for both direct and indirect tunneling process are derived using the Wentzel-Kramers-Brillouin (WKB) approximation for a particle tunneling through the band gap of a semiconductor. The analysis illustrates the exponential decrease in the transmission coefficient as perpendicular momentum increases.

Chapter 3: *Fabrication and Sample Preparation* presents the sample fabrication and bending apparatus used to strain the devices. This chapter also details the silicon polishing etch developed to remove mechanical damage created in the sample sawing process. The polishing etch allows over 50% more stress to applied to the samples before breakage as compared to the unpolished sawed pieces.

The coordinate transformation necessary to calculate the applied strain for stress applied along various crystal directions is described in Chapter 4: *The Stress/Strain Relation*. Since silicon is not an isotropic material, Young's modulus is not constant for stress applied along different crystal directions. More uniaxial stress must be applied along the [110] direction compared to the [100] direction for equal strain to result along the bending direction due to the atomic structure and bond orientation of the crystal.

The experimental data is shown in Chapter 5: *Electrical Measurements and Results*. The current-voltage plot shows a tunneling characteristic for reverse-biases. Three of the four

wafer/strain configurations presented exhibit an increase in current at 1 V reverse bias for compressive strain and a decrease in current for tensile strain: (001) wafer/ $[100]$ strain; (001) wafer/ $[110]$ strain; and (011) wafer/ $[100]$ strain. However the opposite dependence for current and strain is seen for a $(\bar{1}10)$ wafer with $[110]$ strain.

Chapter 6: *Theoretical Current Calculation* details the theoretical calculations for the relative change in tunneling current at 1 V reverse bias. The change in band structure with strain was calculated using the *Band Structure Lab* and *nextnano*[3], and valence band and conduction band parameters were also extracted using these tools. A full-band Poisson solver was created to calculate the energy band diagram for the p-n junction at different strains. The framework for band-to-band tunneling is used to compute the theoretical change in reverse-bias tunneling current versus strain for different wafer/strain configurations. Reasonable agreement is seen between experimental and theoretical results. Lastly, sources of error for the theoretical calculation are discussed.

Appendix A: Procedure for Bonding Strain Gauge to Samples

1. The surface of the test piece was thoroughly cleaned with isopropyl alcohol and allowed to dry.
2. The back edge of the strain gauge was temporarily attached to the surface using general purpose Scotch Tape as shown in Figure 25 below.
3. The un-taped end of the strain gauge was then lifted at about a 30 degree angle, and a couple drops of cyanoacrylate adhesive were placed near the taped end of the strain gauge.
4. The author then used his thumb to apply pressure starting from the taped end working his way forward to the free end of the strain gauge to smooth out the liquid adhesive. While doing this, the author made sure no air bubbles were trapped underneath the strain gauge.

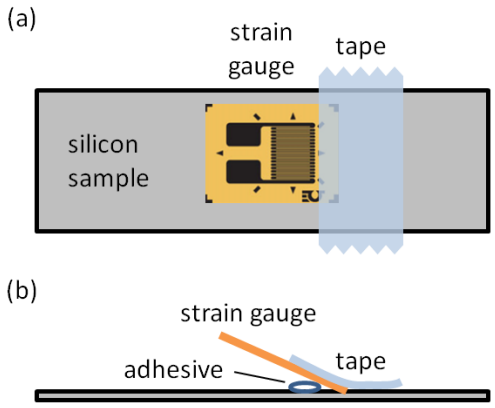

Figure 25. (a) Top-view of strain gauge taped to silicon sample piece. (b) Side-view of the technique used to bond the strain gauge to the silicon sample.

5. With his thumb, constant pressure was applied to the top of the gauge for two minutes so that the adhesive would set.
6. The adhesive was allowed to cure for 24 hours. The tape was then carefully removed from the samples. Care was taken to make sure the strain gauge was not peeled off along with the tape.

Appendix B: Calibration Measurements of the Bending Apparatus

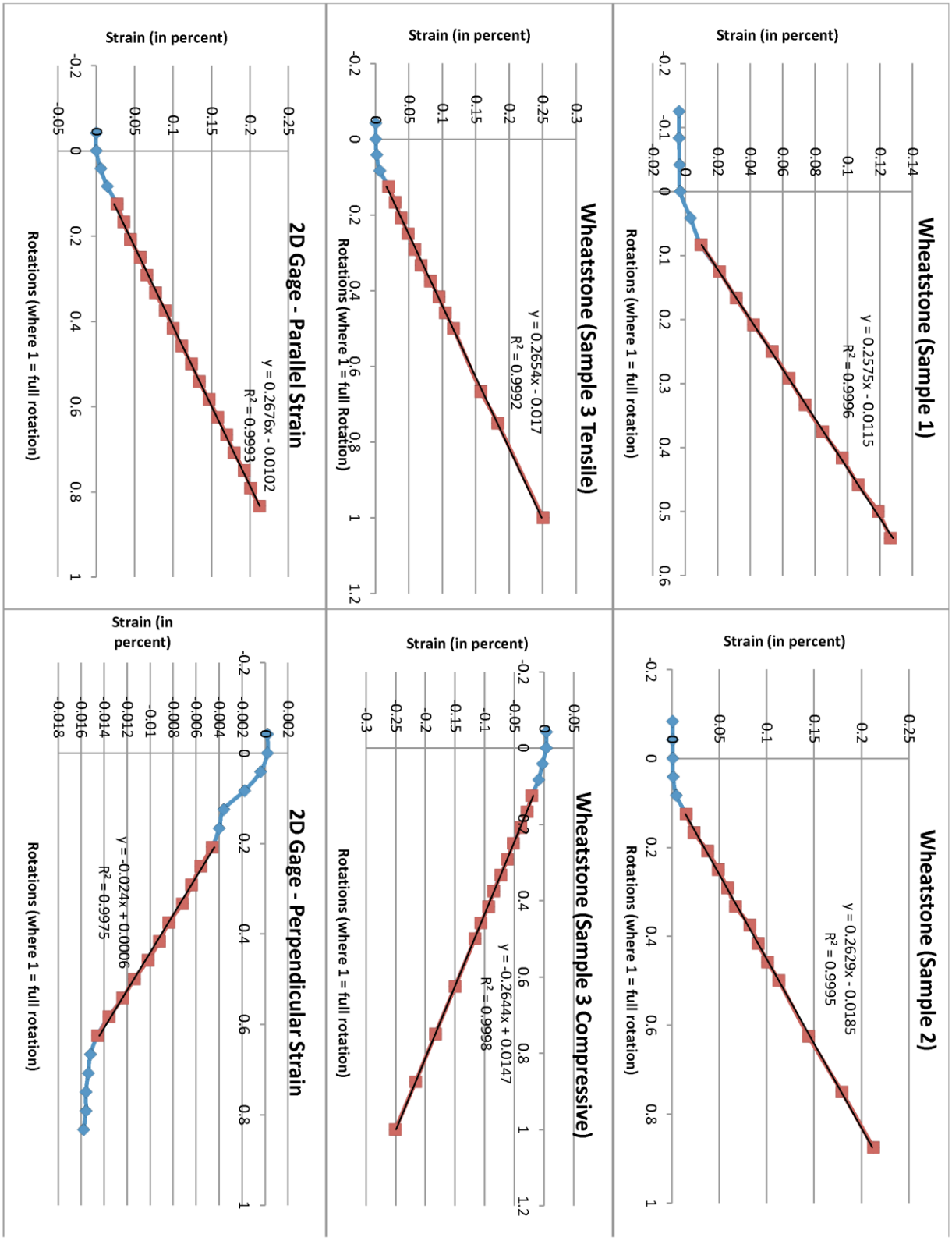

Appendix C: Strain Calculation for Stress Applied Along the [100] Crystal Axis

For this problem, stress is applied along the [100] crystal direction, and stress along all other directions is equal to zero. This is indicated in the table below:

Givens for [100] Applied Stress

$$\begin{bmatrix}\sigma_1\\ \sigma_2\\ \sigma_3\\ \sigma_4\\ \sigma_5\\ \sigma_6\end{bmatrix} \equiv \begin{bmatrix}\sigma_{xx}\\ \sigma_{yy}\\ \sigma_{zz}\\ \sigma_{yz}\\ \sigma_{xz}\\ \sigma_{xy}\end{bmatrix} = \begin{bmatrix}\sigma_{100}\\ 0\\ 0\\ 0\\ 0\\ 0\end{bmatrix}$$

Equation (54) can be easily solved:

[100] applied stress

$$\begin{bmatrix}\epsilon_1\\ \epsilon_2\\ \epsilon_3\\ \gamma_4\\ \gamma_5\\ \gamma_6\end{bmatrix} = \boldsymbol{s}\begin{bmatrix}\sigma_1\\ \sigma_2\\ \sigma_3\\ \sigma_4\\ \sigma_5\\ \sigma_6\end{bmatrix}$$

$$\begin{bmatrix}\epsilon_1\\ \epsilon_2\\ \epsilon_3\\ \gamma_4\\ \gamma_5\\ \gamma_6\end{bmatrix} = \begin{bmatrix}7.68 & -2.14 & -2.14 & 0 & 0 & 0\\ -2.14 & 7.68 & -2.14 & 0 & 0 & 0\\ -2.14 & -2.14 & 7.68 & 0 & 0 & 0\\ 0 & 0 & 0 & 12.6 & 0 & 0\\ 0 & 0 & 0 & 0 & 12.6 & 0\\ 0 & 0 & 0 & 0 & 0 & 12.6\end{bmatrix} \cdot \begin{bmatrix}\sigma_1\\ \sigma_2\\ \sigma_3\\ \sigma_4\\ \sigma_5\\ \sigma_6\end{bmatrix}$$

$$\begin{bmatrix}\epsilon_1\\ \epsilon_2\\ \epsilon_3\\ \gamma_4\\ \gamma_5\\ \gamma_6\end{bmatrix} = \begin{bmatrix}0.768 \cdot \sigma_{100}\\ -0.214 \cdot \sigma_{100}\\ -0.214 \cdot \sigma_{100}\\ 0\\ 0\\ 0\end{bmatrix}$$

(Strain in percent, stress in GPa)

(98)

Appendix D: Coordinate Transformation Calculated for Stress Along the [110] Crystal Axis

In this example, stress is applied along the [110] crystal direction. Following the steps in Section 4.1, *Coordinate Transformation for the Stress/Strain Relation*, the strain and stress in the new and old coordinate system are calculated. The primed coordinate system is drawn in Figure 13, page 44, where x' is directed along the [110] crystal direction, y' is directed along the $[\bar{1}10]$ crystal direction, and z' is directed along the [001] crystal direction.

Givens for [110] Applied Stress

$$\begin{bmatrix}\sigma_1'\\ \sigma_2'\\ \sigma_3'\\ \sigma_4'\\ \sigma_5'\\ \sigma_6'\end{bmatrix} = \begin{bmatrix}\sigma_{110}\\ 0\\ 0\\ 0\\ 0\\ 0\end{bmatrix}$$

$$\boldsymbol{\alpha}_{100\to110} = \begin{bmatrix} 0.5 & 0.5 & 0 & 0 & 0 & 1 \\ 0.5 & 0.5 & 0 & 0 & 0 & -1 \\ 0 & 0 & 1 & 0 & 0 & 0 \\ 0 & 0 & 0 & 0.5\sqrt{2} & -0.5\sqrt{2} & 0 \\ 0 & 0 & 0 & 0.5\sqrt{2} & 0.5\sqrt{2} & 0 \\ -0.5 & 0.5 & 0 & 0 & 0 & 0 \end{bmatrix}$$

(from Equation (68))

$$\boldsymbol{s}' = \begin{bmatrix} 5.91 & -0.368 & -2.14 & 0 & 0 & 0 \\ -0.368 & 5.91 & -2.14 & 0 & 0 & 0 \\ -2.14 & -2.14 & 7.68 & 0 & 0 & 0 \\ 0 & 0 & 0 & 12.6 & 0 & 0 \\ 0 & 0 & 0 & 0 & 12.6 & 0 \\ 0 & 0 & 0 & 0 & 0 & 19.6 \end{bmatrix}, \text{ in } \left(\frac{10^{-12}}{\text{Pa}}\right)$$

(from Table 2)

Strain in the primed coordinate system can be calculated from Equation (67):

[110] applied stress Calculation of strain in the primed coordinate system	$\begin{bmatrix}\epsilon_1'\\ \epsilon_2'\\ \epsilon_3'\\ \gamma_4'\\ \gamma_5'\\ \gamma_6'\end{bmatrix} = \boldsymbol{s}' \begin{bmatrix}\sigma_1'\\ \sigma_2'\\ \sigma_3'\\ \sigma_4'\\ \sigma_5'\\ \sigma_6'\end{bmatrix}$ $\begin{bmatrix}\epsilon_1'\\ \epsilon_2'\\ \epsilon_3'\\ \gamma_4'\\ \gamma_5'\\ \gamma_6'\end{bmatrix} = \begin{bmatrix} 5.91 & -0.368 & -2.14 & 0 & 0 & 0\\ -0.368 & 5.91 & -2.14 & 0 & 0 & 0\\ -2.14 & -2.14 & 7.68 & 0 & 0 & 0\\ 0 & 0 & 0 & 12.6 & 0 & 0\\ 0 & 0 & 0 & 0 & 12.6 & 0\\ 0 & 0 & 0 & 0 & 0 & 19.6\end{bmatrix}\begin{bmatrix}\sigma_1'\\ \sigma_2'\\ \sigma_3'\\ \sigma_4'\\ \sigma_5'\\ \sigma_6'\end{bmatrix}$ $\begin{bmatrix}\epsilon_1'\\ \epsilon_2'\\ \epsilon_3'\\ \gamma_4'\\ \gamma_5'\\ \gamma_6'\end{bmatrix} = \begin{bmatrix} 0.591\cdot\sigma_{110}\\ -0.0368\cdot\sigma_{110}\\ -0.214\cdot\sigma_{110}\\ 0\\ 0\\ 0\end{bmatrix}$ (Strain in percent, stress in GPa)	(99)

In the above equation, stress is given in GPa and strain is calculated in percent $\left(\frac{\Delta L}{L}\cdot 100\right)$. In the equation below, stress is transformed from the primed coordinate system to the unprimed coordinate system:

[110] applied stress Transformation of stress to the unprimed coordinate system	$\begin{bmatrix}\sigma_1\\ \sigma_2\\ \sigma_3\\ \sigma_4\\ \sigma_5\\ \sigma_6\end{bmatrix} = \boldsymbol{\alpha}^{-1}\begin{bmatrix}\sigma_1'\\ \sigma_2'\\ \sigma_3'\\ \sigma_4'\\ \sigma_5'\\ \sigma_6'\end{bmatrix} = \begin{bmatrix}0.5\cdot\sigma_{110}\\ 0.5\cdot\sigma_{110}\\ 0\\ 0\\ 0\\ 0.5\cdot\sigma_{110}\end{bmatrix}$	(100)

Lastly, strain in the unprimed coordinate system, which is aligned with the crystal axis is calculated below:

[110] applied stress Transformation of strain to the unprimed coordinate system	$\begin{bmatrix}\epsilon_1\\ \epsilon_2\\ \epsilon_3\\ \gamma_4\\ \gamma_5\\ \gamma_6\end{bmatrix} = \boldsymbol{\alpha}^T \begin{bmatrix}\epsilon_1'\\ \epsilon_2'\\ \epsilon_3'\\ \gamma_4'\\ \gamma_5'\\ \gamma_6'\end{bmatrix} = \boldsymbol{\alpha}^T \begin{bmatrix}0.591 \cdot \sigma_{110}\\ -0.0368 \cdot \sigma_{110}\\ -0.214 \cdot \sigma_{110}\\ 0\\ 0\\ 0\end{bmatrix} = \begin{bmatrix}0.277 \cdot \sigma_{110}\\ 0.277 \cdot \sigma_{110}\\ -0.214 \cdot \sigma_{110}\\ 0\\ 0\\ 0.628 \cdot \sigma_{110}\end{bmatrix}$ (Strain in percent, stress in GPa)	(101)

Appendix E: Comparison of Strained Band Structure Simulations

Shown below are calculations using three different codes to calculate band structure.

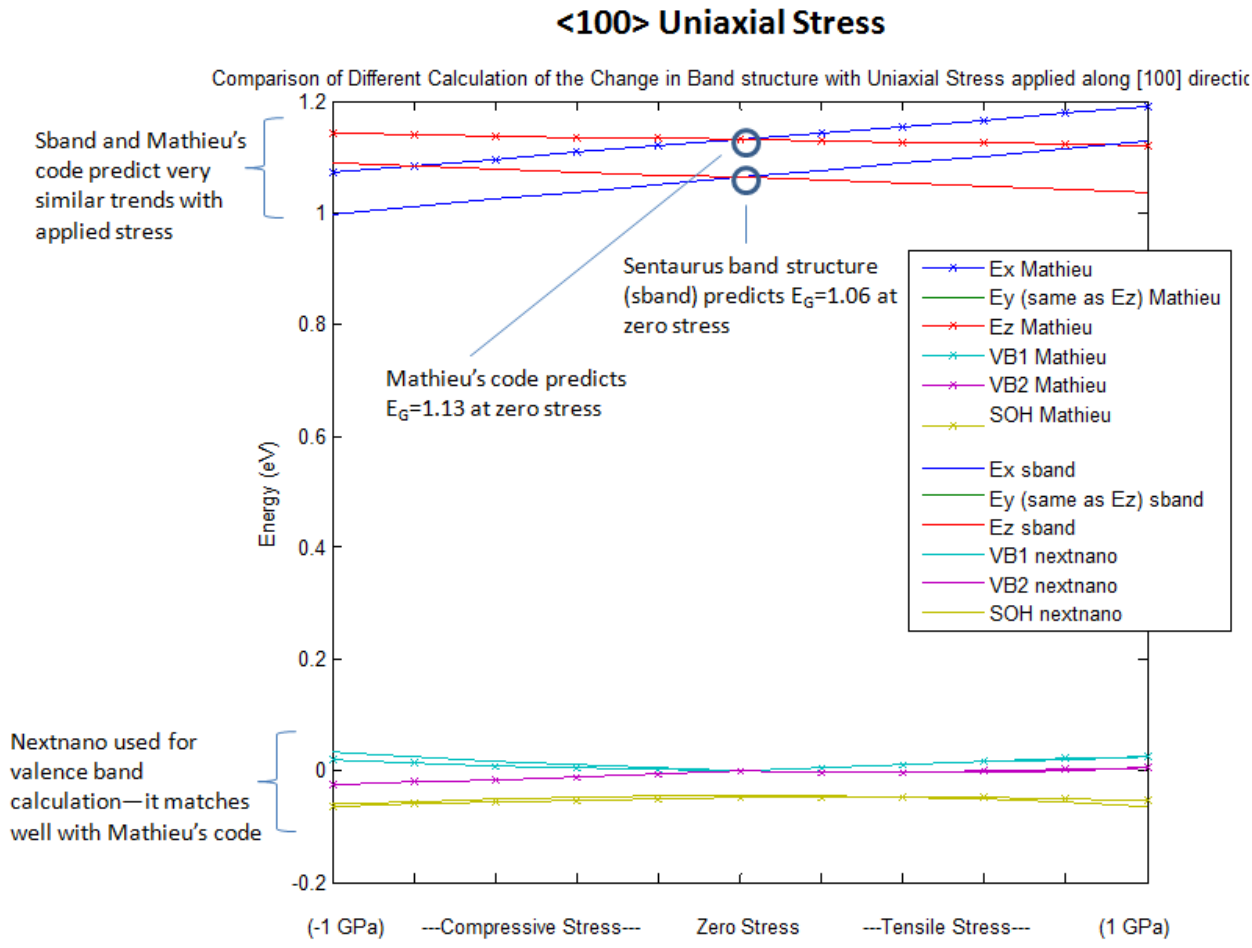

Figure 26. Comparison of band structure simulations for <100> directed uniaxial stress.

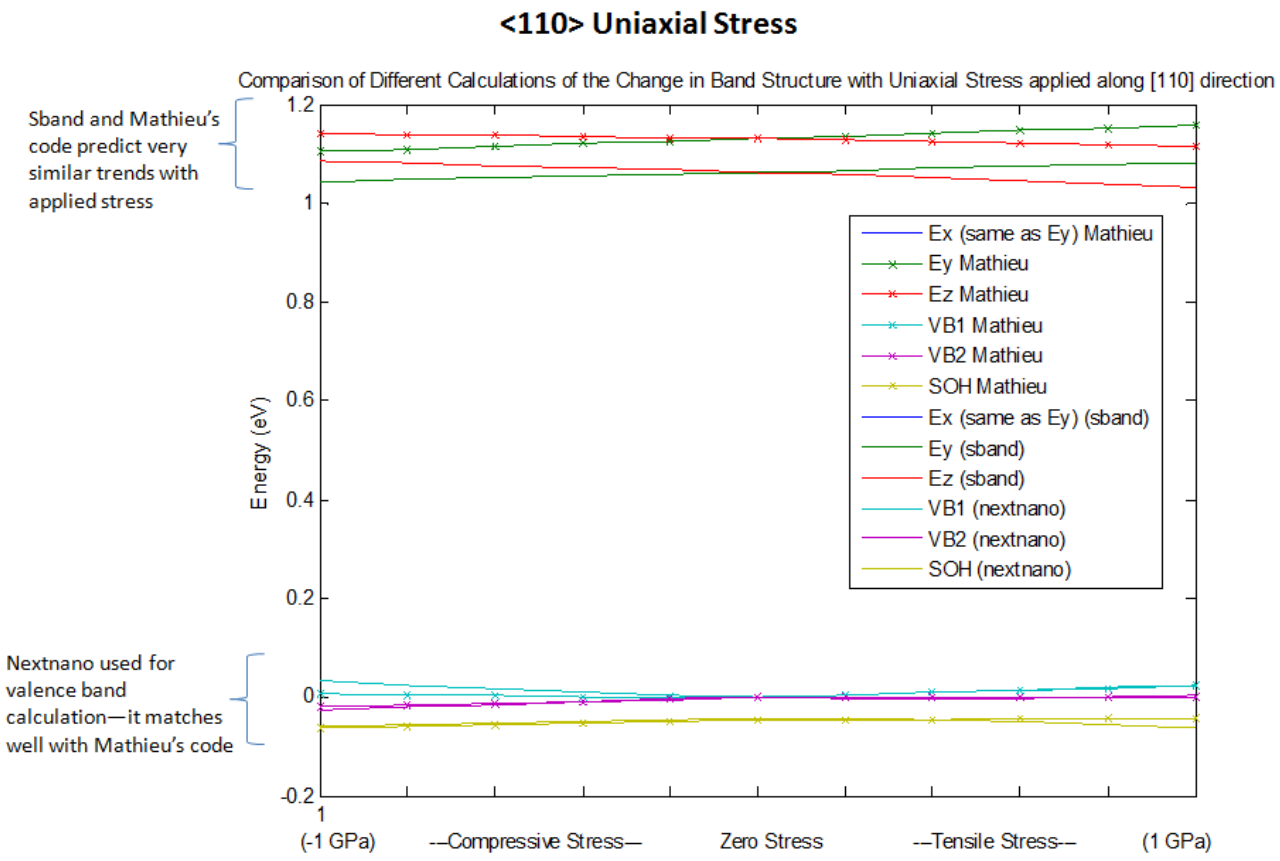

Figure 27. Comparison of band structure simulations for <110> directed uniaxial stress.

Appendix F: Valence Band *E-k* Diagrams

Shown below is the *E-k* diagram for the top valence band with $k_z = 0$ and zero stress applied.

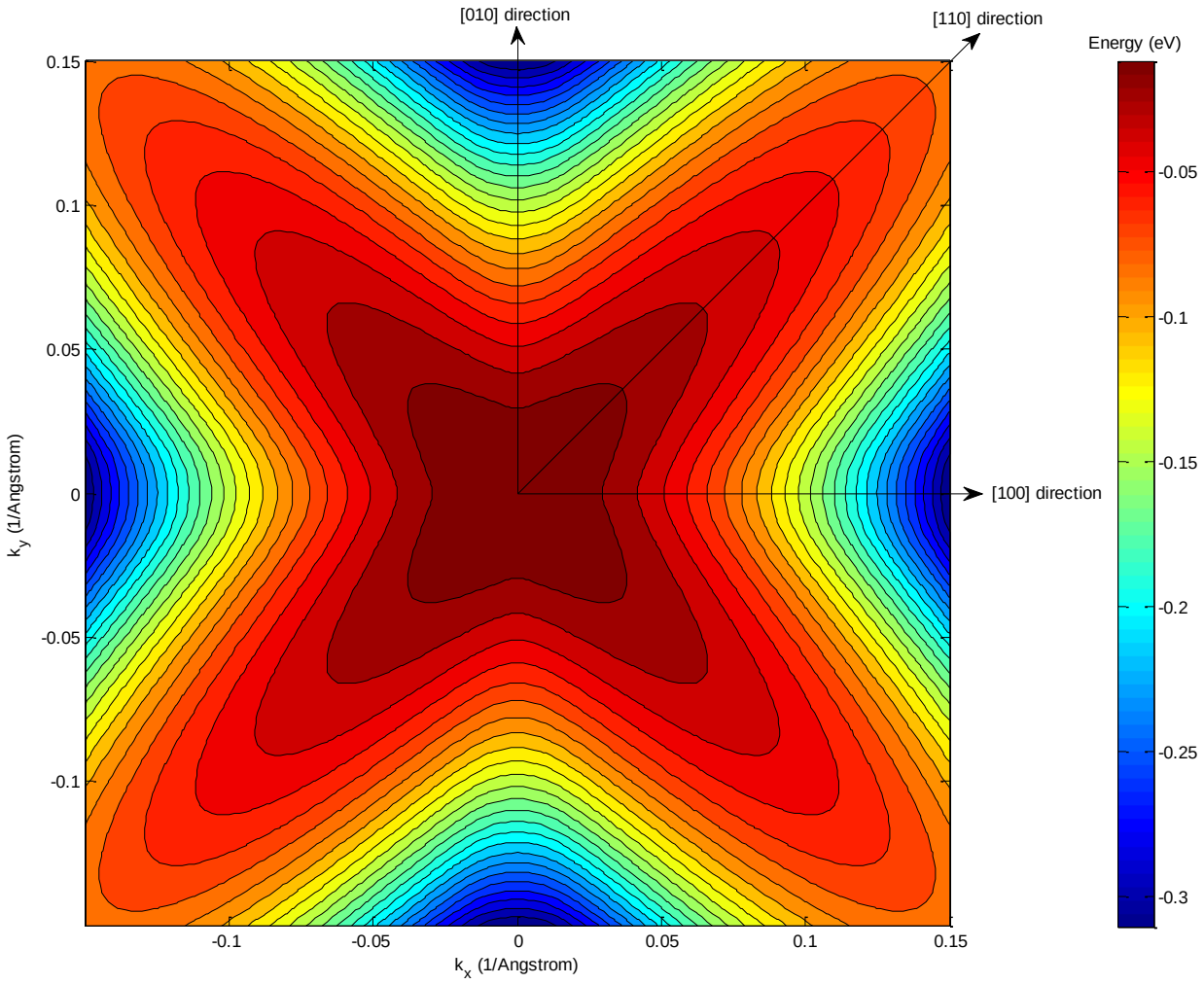

Figure 28. Valence band *E-k* with zero stress applied, calculated by *nextnano*[3].

References

[1] R.H. Dennard, F.H. Gaensslen, V.L. Rideout, E. Bassous, and A.R. LeBlanc, "Design of ion-implanted MOSFET's with very small physical dimensions," *IEEE Journal of Solid-State Circuits*, vol. 9, 1974, pp. 256–268.

[2] T. Ghani, M. Armstrong, C. Auth, M. Bost, P. Charvat, G. Glass, T. Hoffmann, K. Johnson, C. Kenyon, J. Klaus, B. McIntyre, K. Mistry, A. Murthy, J. Sandford, M. Silberstein, S. Sivakumar, P. Smith, K. Zawadzki, S. Thompson, and M. Bohr, "A 90nm high volume manufacturing logic technology featuring novel 45nm gate length strained silicon CMOS transistors," *Electron Devices Meeting, 2003. IEDM '03 Technical Digest. IEEE International*, 2003, pp. 11.6.1-11.6.3.

[3] K. Mistry, C. Allen, C. Auth, B. Beattie, D. Bergstrom, M. Bost, M. Brazier, M. Buehler, A. Cappellani, R. Chau, C. Choi, G. Ding, K. Fischer, T. Ghani, R. Grover, W. Han, D. Hanken, M. Hattendorf, J. He, J. Hicks, R. Huessner, D. Ingerly, P. Jain, R. James, L. Jong, S. Joshi, C. Kenyon, K. Kuhn, K. Lee, H. Liu, J. Maiz, B. Mclntyre, P. Moon, J. Neirynck, S. Pae, C. Parker, D. Parsons, C. Prasad, L. Pipes, M. Prince, P. Ranade, T. Reynolds, J. Sandford, L. Shifren, J. Sebastian, J. Seiple, D. Simon, S. Sivakumar, P. Smith, C. Thomas, T. Troeger, P. Vandervoorn, S. Williams, and K. Zawadzki, "A 45nm Logic Technology with High-k+Metal Gate Transistors, Strained Silicon, 9 Cu Interconnect Layers, 193nm Dry Patterning, and 100% Pb-free Packaging," *Electron Devices Meeting, 2007. IEDM 2007. IEEE International*, 2007, pp. 247-250.

[4] Chenming Hu, "Green transistor as a solution to the IC power crisis," *Solid-State and Integrated-Circuit Technology, 2008. ICSICT 2008. 9th International Conference on*, 2008, pp. 16-20.

[5] P.M. Solomon, S.E. Laux, L. Shi, J. Cai, and W.E. Haensch, "Experimental and theoretical explanation for the orientation dependence gate-induced drain leakage in scaled MOSFETs," *Device Research Conference*, 2009.

[6] J. Appenzeller, J. Knoch, M.T. Bjork, H. Riel, H. Schmid, and W. Riess, "Toward Nanowire Electronics," *IEEE Transactions on Electron Devices*, vol. 55, 2008, pp. 2827-2845.

[7] S. Jin, M.V. Fischetti, and E. Lyumkis, "Nonlocal band-to-band tunneling model for multidimensional device simulators," *Journal of Applied Physics*, 2009.

[8] A. Karalis, J. Joannopoulos, and M. Soljacic, "Efficient wireless non-radiative mid-range energy transfer," *Annals of Physics*, vol. 323, Jan. 2008, pp. 34-48.

[9] Ioffe Physical Technical Institute, "Physical Properties of Semiconductors."

[10] Abhijeet Paul, Mathieu Luisier, Neophytos Neophytou, Raseong Kim, Junzhe Geng, Michael McLennan, Mark Lundstrom, and Gerhard Klimeck, "Band Structure Lab," May. 2006.

[11] Wikipedia, “Image of first Brillouin zone of an FCC lattice.”

[12] N. Holonyak, I.A. Lesk, R.N. Hall, J.J. Tiemann, and H. Ehrenreich, “Direct Observation of Phonons During Tunneling in Narrow Junction Diodes,” *Physical Review Letters*, vol. 3, 1959, p. 167.

[13] P.L. Hagelstein, S.D. Senturia, and T.P. Orlando, *Introductory applied quantum and statistical mechanics*, Wiley-IEEE, 2004.

[14] D.K. Ferry, *Quantum Mechanics: An Introduction for Device Physicists and Electrical Engineers*, CRC Press, 2001.

[15] P.M. Solomon, J. Jopling, D.J. Frank, C. D'Emic, O. Dokumaci, P. Ronsheim, and W.E. Haensch, “Universal tunneling behavior in technologically relevant P/N junction diodes,” *Journal of Applied Physics*, vol. 95, May. 2004, pp. 5800-5812.

[16] B. Schwartz and H. Robbins, “Chemical Etching of Silicon,” *Journal of the Electrochemical Society*, Dec. 1976.

[17] M. Steinert, J. Acker, M. Krause, S. Oswald, and K. Wetzig, “Reactive Species Generated during Wet Chemical Etching of Silicon in HF/HNO3 Mixtures,” *The Journal of Physical Chemistry B*, vol. 110, Jun. 2006, pp. 11377-11382.

[18] S. Thompson and others, “Flexure Based Wafer Bending Setup User's Guide.”

[19] Omega Engineering, Inc., “Uniaxial Strain Gages.”

[20] Wikipedia, “Image of wheatstone bridge.”

[21] S. Birner, “Nextnano3 Keyword Glossary.”

[22] R.F. Tinder, *Tensor properties of solids*, Morgan & Claypool Publishers, 2008.

[23] W.A. Brantley, “Calculated elastic constants for stress problems associated with semiconductor devices,” *Journal of Applied Physics*, vol. 44, 1973, p. 534.

[24] S. Birner, S. Hackenbuchner, M. Sabathil, G. Zandler, J.A. Majewski, T. Andlauer, T. Zibold, R. Morschl, A. Trellakis, and P. Vogl, “Modeling of Semiconductor Nanostructures with nextnano^3,” *ACTA PHYSICA POLONICA SERIES A*, vol. 110, 2006, p. 111.

[25] Synopsys, “Sentaurus Device Monte Carlo User Guide.”

[26] Y. Kanda, “Effect of Stress on Germanium and Silicon p-n Junctions,” *Japanese Journal of Applied Physics*, vol. 6, 1967, pp. 475-486.

[27] S.E. Laux, “Computation of Complex Band Structures in Bulk and Confined Structures.”